UNIVERSITY OF OKLAHOMA

GRADUATE COLLEGE

SEISMIC RADIATION DURING SLIP ALONG BI-MATERIAL FAULTS: AN EXPERIMENTAL INVESTIGATION

A THESIS

SUBMITTED TO THE GRADUATE FACULTY

in partial fulfillment of the requirements for the

Degree of

MASTER OF SCIENCE

By

TANNER SHADOAN
Norman, Oklahoma
2019

SEISMIC RADIATION DURING SLIP ALONG BI-MATERIAL FAULTS:
AN EXPERIMENTAL INVESTIGATION

A THESIS APPROVED FOR THE
CONOCOPHILLIPS SCHOOL OF GEOLOGY AND GEOPHYSICS

BY

Dr. Brett M. Carpenter, Chair

Dr. Ze'ev Reches

Dr. Xiaowei Chen

Acknowledgements

I would first like to thank Dr. Brett M. Carpenter, without whom the following pages would not be possible. Dr. Carpenter has pushed, challenged, and strengthened my knowledge in the geosciences and has always been available to give insightful and relevant advice to my research and master's thesis. Furthermore, I would like to thank Dr. Ze'ev Reches and Dr. Xiaowei Chen for their knowledgeable insights on the following research allowing for it to be clear and robust. I would also like to thank Xiaofeng Chen and Simon Zu for the continuous help they have provided me in the lab. Lastly, I would like to thank Folarin Kolawole, Will Kibikas, and Christina Hamilton for giving me feedback on various ideas, presentations, and papers.

Table of Contents

List of Tables

List of Figures

Abstract

Large slip along faults is likely to place crustal blocks of different lithological and mechanical properties against one another, a process that forms a bi-material fault. To explore the behavior of such faults, I conducted shear experiments on bimaterial-faults and analyzed the characteristics of laboratory earthquakes. The experimental faults were composed of two blocks of gabbro, dolomite, and sandstone, forming nine lithological combinations. The blocks were in contact by a ring-shaped fault and were loaded in a rotary shear apparatus (ROGA) at the University of Oklahoma. Slip rates and normal stresses ranged from 0.25μm/s to 1cm/s and 0.5 to 15 MPa, respectively. I performed constant velocity experiments and monitored the seismic radiation, via acoustic emissions, along the fault surface with four 3D accelerometers mounted ~2 cm away from the experimental fault at a rate of 1 MHz.

I analyzed acoustic emissions (laboratory earthquakes) using traditional seismological techniques. The experiments show distinct dependence of seismic radiation on (1) the mechanical contrast between the two blocks that controls the rupture characteristics, and (2) the mechanical properties of the blocks that control the nature of the ray path of the acoustic waves. For example, the Gutenberg-Richter relationship revealed that experiments containing gabbro and dolomite, a bi-material fault, have intermediate behavior and mimic both end members of the single lithology faults of gabbro and dolomite. Furthermore, frequency spectrum data revealed the differences in seismic radiation due to rupture and ray path characteristics. For example, for an experimental fault composed of gabbro and sandstone, the recorded events on the more compliant side (sandstone) of the fault have low amplitudes (low accelerations) at higher frequencies. I deduced that the ray path, which is controlled by the rock properties, is responsible for this difference. The analysis showed that while keeping the ray path constant (i.e. dolomite)

but changing the other fault rock, to either gabbro, sandstone, or dolomite, will still observe differences in the frequency content, this time due to rupture characteristics of the laboratory earthquakes.

The experiments show the distinct dependence of seismic radiation on the mechanical properties of the fault lithologies and their contrast. Further, they indicate that the nature of a bimaterial fault has strong control on the mechanisms of fault rupture and the frequency content of seismic radiation.

Chapter 1 Introduction

Natural Bi-material Faults

Large-displacement faults likely bring into contact crustal blocks of different lithology and mechanical properties; this arrangement is referred to as a bi-material fault. One example of a bi-material fault is the Punchbowl fault in Southern California, which has 44 km of right-lateral slip and has brought into contact crystalline basement and the Punchbowl formation (Figure 1.1; Dibblee & Minch, 2002). In this case, the southern fault block is composed of diorite, quartz monzonite, and gneissic rocks which are in contact with the northern fault block composed of pebbly arkosic sandstone with interbedded siltstones (Chester, et al., 2005).

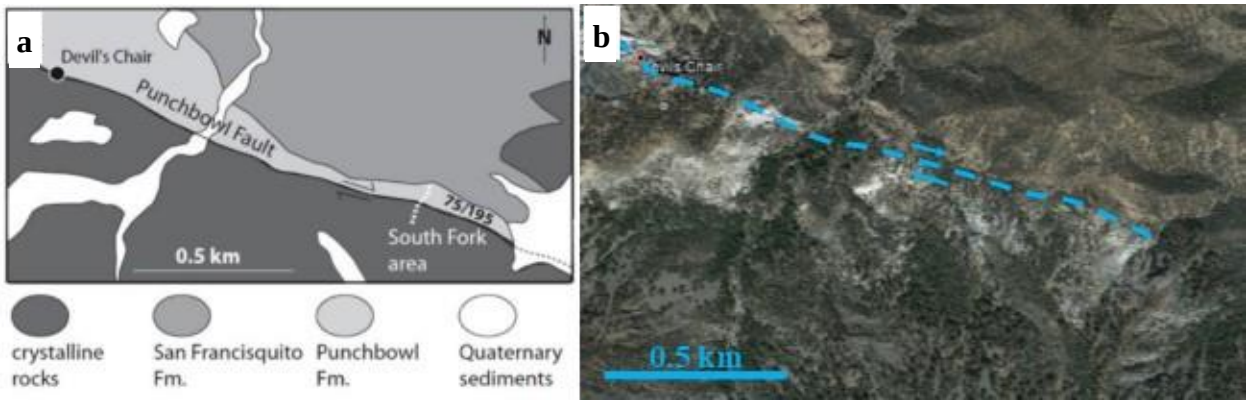

Figure 1.1 (a) Geologic map of the Punchbowl fault (modified from Dibblee & Minch, 2002). (b) Satellite image of the Punchbowl fault. The Punchbowl fault is a bi-material fault and the images show the different colors (i.e. different lithology) on either side of the fault.

Bi-material faults are not exclusive to the juxtaposition of contrasting lithologies; rather any fault with blocks of dissimilar mechanical properties (i.e. shear modulus and seismic wave velocities) may be considered a bi-material fault. Factors such as lithology, porosity, liquid/gas content, fault zone width, etc. control mechanical properties of fault blocks, which cause dissimilar mechanical properties and therefore a bi-material fault.

Monitoring fault zone head waves from earthquakes along the Hayward fault in Southern California have allowed for the observation of the bi-material interface (Allam, et al., 2014). On the seismically fast side of the fault, earthquake seismograms had relatively uniform first peaks with consistent first arrivals, while on the seismically slow side of the fault, earthquake seismograms had varying first arrival times before the first major peak (Figure 1.2, Allam, et al., 2014). The difference in the seismic radiation is due to the bi-material contact of the Hayward Fault. Similar studies have observed bi-material faults in the subsurface such as the North Anatolian fault in northern Turkey (Najdahmadi, et al., 2016; Ozakin, et al., 2012; Bulut, et al., 2012) and the Garzê-Yushu fault in China (Yang, et al., 2015). These studies, along with field outcrops (i.e. Punchbowl fault), geophysical logs (Townend, et al., 2013), and seismic tomography images (Thurber, et al., 2006) show that bi-material faults are typical of large displacement strike-slip faults and are observed worldwide.

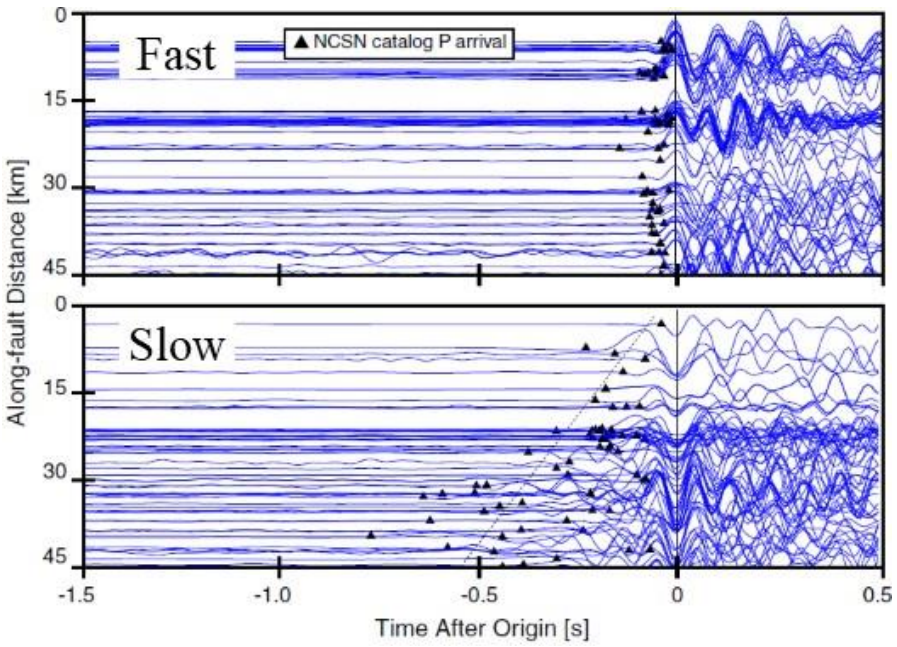

Figure 1.2 Seismograms from two stations on either side of the Hayward fault in southern California. The fault is bi-material; one station recorded earthquakes on the seismically fast side of the fault, while the other recorded earthquakes on the seismically slow side of the fault (modified from Allam et al., 2014).

Theoretical Research

Theoretical studies along bi-material faults have mostly been dedicated to earthquake physics. Weertman (1980) showed that unstable slip is possible along a bi-material interface. Later research has shown that bi-material faults have distinct effects on the earthquake characteristics; including, a preferred propagation direction on dynamic rupture (Ampuero & Ben-Zion, 2008; Brietske, et al., 2007; Andrews & Ben-Zion, 1997), asymmetric distribution of aftershocks (Rubin & Ampuero, 2007; Zaliapin & Ben-Zion, 2011), supershear rupture (Xia, et al., 2005), asymmetric fault damage (Dor, et al., 2006; Rempe, et al., 2013) and asymmetric ground motion (Brietzke, et al., 2009; Ben-Zion, 2002; Shi & Ben-Zion, 2009). Additionally, bi-material interfaces along dip-slip faults show that the stress-drop depends on the location of the compliant block (Ma & Beroza, 2008). Further, ground shaking models along the San Andreas fault (Olsen, et al., 2006), along with these numerical models, show that bi-material faults affect rupture velocity and seismic radiation efficiency, and therefore, may affect local seismic hazards.

Experiments on Laboratory Faults

The practical limitations of monitoring earthquakes at high rates close to the source restrict the understanding of earthquake physics. Research of experimental faults in the laboratory allows for monitoring key parameters close to a fault during slip. Typical experiments are done by shearing different materials against one another while monitoring friction, shear stress, normal stress, strain, and acoustic emissions.

Previous Studies

A number of experimental analysis have been devoted to bi-material faults using a combination of modeling materials, such as homalite, polycarbonate, PMMA (polymethylmethacrylate), steel, and foam rubber (Xia, et al., 2005; Shlomai & Fineberg, 2016;

Lykotrafitis & Rosakis, 2006; Langer, et al., 2013; Anooshehpoor & Brune, 1999). The shearing of these materials has shown wrinkle-like pulses and supershear rupture, which have confirmed the numerical predictions of Weertman (1980) and Andrews & Ben-Zion (1997). Although it is important to show that experiments and numerical modeling are in parallel, the materials used in these experiments may differ from geologic material. Relevant geological material (i.e. sedimentary, carbonates, and crystalline rocks) add complexities to elastic and failure mechanisms due to rock granularity and heterogeneities.

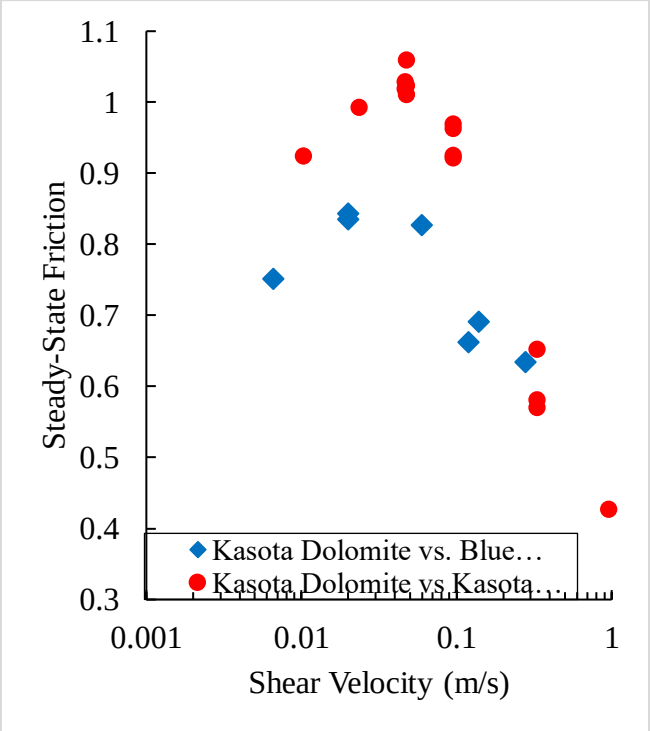

Figure 1.3 Steady-state friction vs shear velocity comparing a single lithology fault and a bi-material fault. The two experimental fault configurations show contrasting frictional behaviors due to the fault lithologies (data derived from Boneh et al., 2013).

There have been few experimental analyses with bi-material faults using rocks. Moore et al. (2010) found that hydrothermal shearing of serpentine and granite was weaker than expected, because of the solution transfer of minerals at grain-to-grain contacts. Boneh et al. (2013) sheared dolomite against dolomite and dolomite against quartzite to find that the two combinations have different behavior in velocity-dependent friction (Figure 1.3). These

experiments along bi-material faults show that using rock samples may create complex fault mechanisms that are not necessarily explained by numerical models. Therefore, the present work is a comprehensive study of slip along experimental bi-material faults using rock blocks.

The Present Study

Objective

The objective of this study is to characterize the acoustic emissions along bi-material faults by conducting shear experiments along both single lithology and bi-material faults while recording acoustic emissions. I analyzed the acoustic emissions using statistical methods and characterizing frequency spectrum content to give insight on the mechanics of fault rupture.

Organization

Chapter 1, Introduction presented a definition of bi-material faults with natural, theoretical, and experimental examples. The chapter explained the need of a more comprehensive study along experimental bi-material faults that use rock blocks.

Chapter 2, Methodology presents the methods used in the experiments, including a detailed explanation of the apparatus, samples, experimental conditions, and analytical methods used to study the acoustic emissions.

Chapter 3, Frequency-Magnitude Analysis of Acoustic Emissions presents the results of the statistical analysis of the acoustic emissions in the experiments. I discuss the implications rock samples have on the recorded acoustic emissions, by showing the strength of chatter in sandstone experiments and showing the relationship between occurrence and event size.

Chapter 4, Frequency Spectrum Analysis is an in-depth analysis of the acoustic emissions, by looking at the waveforms of single events. I will relate their behavior back to

source effects and ray propagation path. This analysis is done by using the frequency spectrum and spectrograms.

Chapter 5, Summary synthesizes chapters 1-4 and is a final summary on how this thesis adds to previous studies along bi-material faults.

Chapter 2 Methodology

Experimental Setup

ROtary Gouge Apparatus (ROGA)

I conducted experiments in a rotary apparatus at the University of Oklahoma, called ROGA (ROtary Gouge Apparatus, Figure 2.1) that can shear and monitor fault behavior assuming to simulate earthquake shear (Reches & Lockner, 2010). ROGA has two massive decks and is supported by a 1.8 m tall frame. Experimental samples are composed of solid blocks that are then placed between the decks. ROGA is equipped with a piston that has the capability to apply a normal stress of up to 35 MPa and two motors that have the capability to shear at velocities between 0.25 μm/s to 2 m/s. Furthermore, there are multiple monitoring instruments around the sample that record normal stress, shear stress, shear velocity/displacement, friction, dilation, compaction, and acoustic emissions. With the use of the encoder signal, the timing of these parameters is synchronized. ROGA's other capacities are explained in Reches and Lockner (2010).

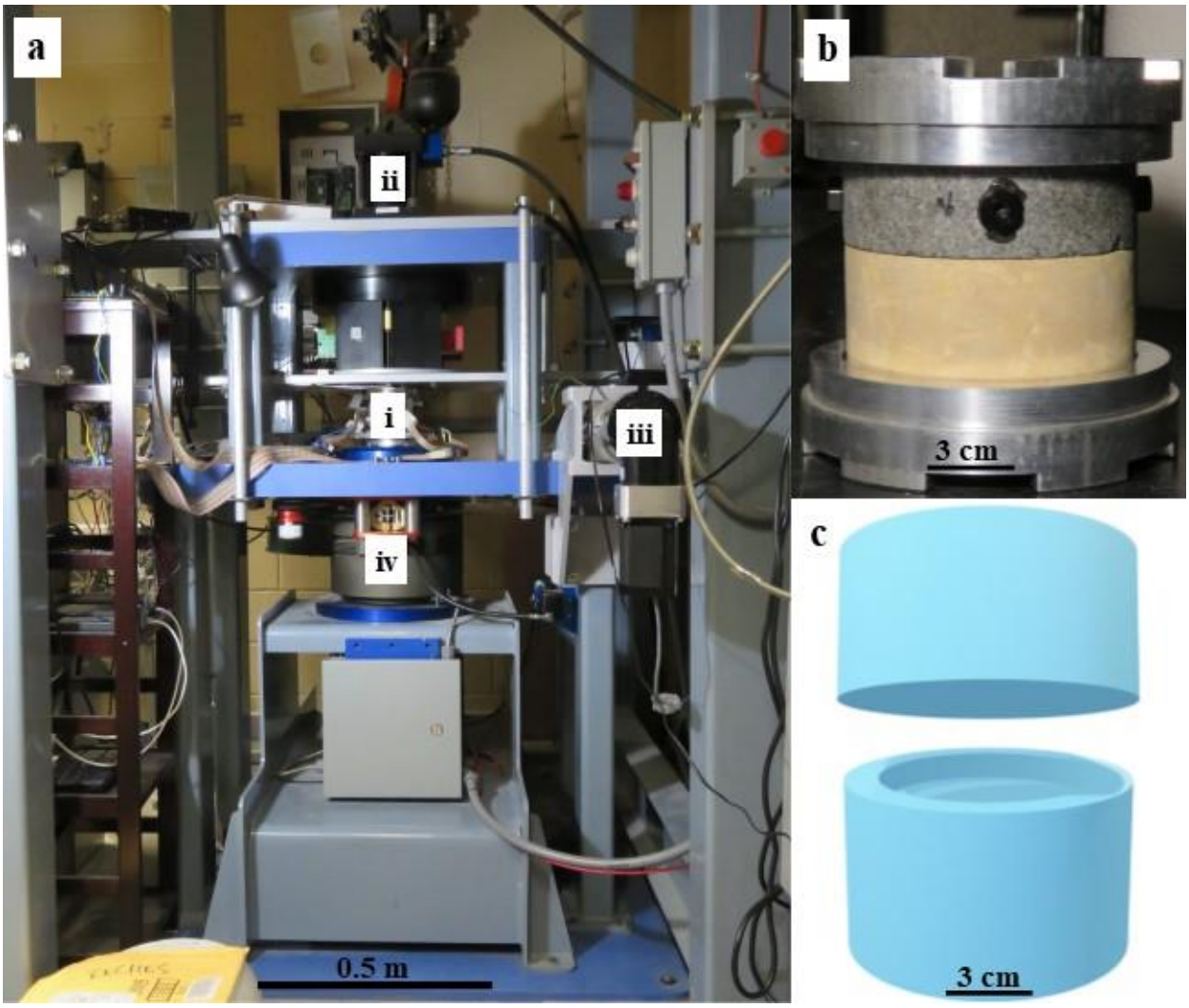

Figure 2.1 (a) Image of ROGA (ROtary Gouge Apparatus) showing sample placement (i), the piston (ii), the slow motor (iii), and the original motor behind the apparatus (iv). (b) Example of stacked rock blocks (i.e. gabbro on dolomite) glued into metal sample holders. (c) Model of the two experimental configurations.

Rock Samples

I used three samples in the experiments that are sourced from Coldspring USA: Raven Noir Granite, Kasota Valley Limestone, and Dunnville Sandstone. For the remainder of the document, I refer to these commercial names as gabbro, dolomite, and sandstone, respectively. These three samples cover a wide range of lithologies and mechanical properties (summarized in Table 2.1). The bulk density (p), P-wave (v_p), and S-wave (v_s) data for each lithology was collected by Will Kibikas at the University of Oklahoma. The bulk density for each lithology is

calculated by measuring the samples' dimensions and mass. The P-wave (v_p) and S-wave (v_s) velocities are determined by using the pulse transmission method (Mattaboni & Schreiber, 1967) at 2 MPa. Each lithology was placed between two steal caps with mounted P-wave and S-wave piezoelectric transducers on each cap. A pulse is generated through the experimental sample and a Tektronix MDO3022 oscilloscope records the P- and S-waves. The difference in first arrivals, along with distance between the caps, provides the P-wave and S-wave velocities. Shear modulus and Poisson's ratio were calculated from these velocities using equations: $\mu = pv_s^2$ and $\sigma = {}^1\!/_2 \, \frac{v_p^2/v_s^2 - 2}{v_p^2/v_s^2 - 1}$, respectively. The gabbro is the strongest and stiffest, followed by dolomite, then sandstone as the weakest one.

Table 2.1 Mechanical properties of experimental samples

Samples[1]	P-wave velocity[2] (v_p, m/s)	S-wave velocity[2] (v_s, m/s)	Bulk Density[2] (p, g/cm^3)	Shear Modulus[3] (μ, GPa)	Poisson's Ratio[3] (σ)	Compressive strength[4] (MPa)
Gabbro	6760	4450	3.1	61	0.116	291
Dolomite	4490	2420	2.5	18	0.295	39
Sandstone	2710	1690	1.8	14	0.181	17

[1] Sourced from Coldspring USA as Raven Noir Granite, Kasota Valley Limestone, and Dunnville Sandstone, respectively.
[2] Measured at the University of Oklahoma in the Rock Mechanics Laboratory
[3] Calculated from measured v_p, v_s, p,
[4] (Data from Coldspring USA, 2019)

The two solid rock blocks are stacked on top of each other (Figure 2.1b) with a ring interface and loaded into the apparatus. There are two designs for the rock blocks (Figure 2.1c); the first is a 5 cm tall cylindrical block that is 10.2 cm in diameter. The second design is like the first, but with a 1.2 cm thick raised ring on the outer edge of the block that adds 0.7 cm to the height. The block surfaces are parallel ground to create a flat surface then roughened using 400 grit powder. The rock samples are placed and epoxied into metal sample holders. The loading shear motor is only attached to the lower block and the upper block is stationary. It is important

to note that the accelerometers (explained in detail below) are attached only to the stationary upper block (Figure 2.1b). With three lithologies and two rock block designs, there are six types of rock blocks and nine rock block combinations. In other words, each lithology (i.e. gabbro, dolomite, and sandstone) has two rock blocks (i.e. flat cylindrical block and flat cylindrical block with a raised ring, Figure 2.1c); thus, there are a total of nine combinations. All fault blocks and their combinations are illustrated in Figure A.1. Furthermore, refer to Appendix D for a complete list of experiments and experimental conditions.

3D-Accelerometers

The accelerometer system includes:

(1) four accelerometers from PCB Piezotronics, model 356B21; they have the capability to record in all three spatial dimensions (a total of 12 channels) with a range of ± 5 volts,

(2) three signal conditioners from PCB Piezotronics, model 482C15 with four channels each,

(3) four Ultra-High-Speed Multifunction PCI Board, model PCI-DAS4020/12 with 4 channels each, all sampling at rate of 1 MHz.

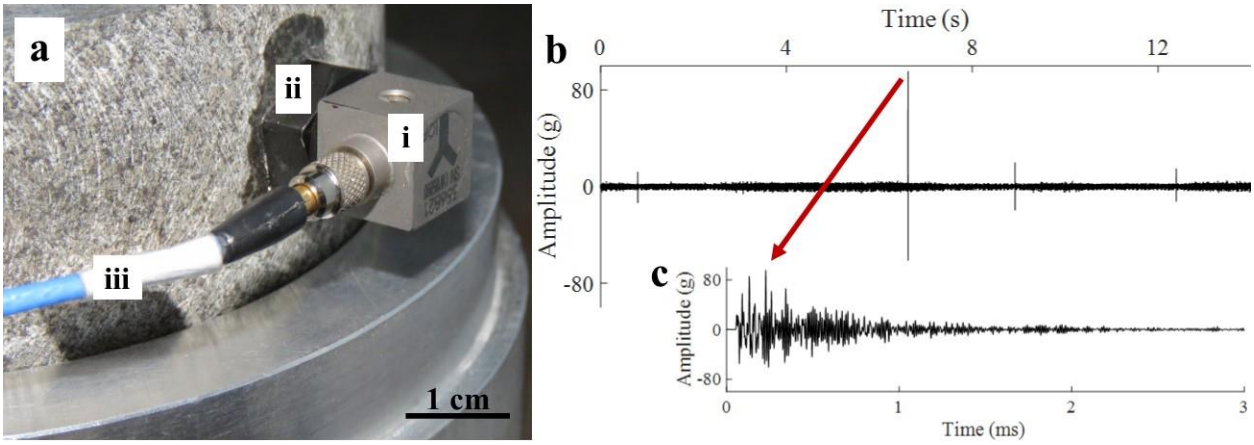

Figure 2.2 (a) Image of the accelerometer (i), also including the accelerometer mount (ii) and the cable connecting to the computer (iii). (b) Accelerogram of the acoustic emissions recording during shear. (c) Accelerogram of one acoustic event showing the similarity to a natural earthquake. The red arrow shows the peak amplitude of the event. Notice the time units on both plots; acoustic events only last for ~3ms.

Four 3D-accelerometers are attached to the upper block to record acoustic emissions. The accelerometers (Figure 2.2a) are screwed onto mounts that are epoxied to the side of the stationary block at equal spaces and ~2 cm from the fault surface. Each accelerometer is mounted to align so that the X, Y, and Z directions are parallel to shear, transverse to shear, and normal to the fault, respectively. The mounts are traced onto the side of the sample 90° apart and equal distance from the fault. Each accelerometer is mounted at the same relative position to remain aligned from experiment to experiment. Besides the accelerometer channels, each PCI board is connected to the same encoder, which allows for synchronization of the four boards and other mechanical data.

The four accelerometers act as mini seismic-stations that record laboratory earthquakes or acoustic emissions that are created during shear. As with natural earthquakes, the acoustic emissions are plotted on accelerograms (Figure 2.2b), while individual "spikes" on the recorded accelerograms are termed acoustic events (AEs, Figure 2.2c). The accelerometers record the acoustic emission in volts, but the accelerometers have been calibrated so that 1 volt equals 100g. These acoustic events have similar characteristics to natural earthquakes; therefore, I used seismological techniques to study the acoustic events; such as:

(1) Root Mean Square (RMS) of seismic-chatter (The MathWorks, Inc., 2019)

(2) Relationship between occurrence (N) and peak amplitude (PA) of distinct events (Gutenberg & Richter, 1944).

(3) Frequency spectrum and spectrograms

Analysis

RMS of Chatter

Depending on the behavior of the acoustic emissions, I analyzed the data using two methods. For acoustic emissions with low amplitude and chatter-like behavior, I calculate the root mean square (RMS, The MathWorks, Inc., 2019)

$$RMS = \sqrt[2]{\frac{1}{n}(a_1^2 + a_2^2 + \ldots + a_n^2)},$$

where RMS is in g (acceleration due to gravity), n is the number of data samples in the acoustic emission recording of the experiment, and a is the amplitude in g. I used the RMS values to define the strength of the low amplitude, chatter-like behavior. Similarly, RMS of seismic data was calculated as a statistical parameter that identified continuous chatter of the Cascadia subduction zone that was revealed by machine learning (Rouet-Leduc, et al., 2019). I also characterized background noise levels by calculating the RMS of a sandstone-sandstone experiment prior to the motor initiating, which resulted in a value of 0.19 g (Figure 2.3).

Occurrence vs Peak Amplitude Plots

For acoustic emissions with high amplitude, distinct, impulsive events, I show the relationship between the magnitude and the cumulative frequency, which is referred to as the Gutenberg-Richter relationship (Gutenberg & Richter, 1944). Typically, Richter magnitude of earthquakes are calculated using the distance travelled from rupture source to seismic station (Richter, 1935). The experimental system does not have the capability to accurately locate the acoustic events or determine their magnitude due to the number of accelerometers. Therefore, I use the peak amplitude (PA, Figure 2.2) to define the size of the acoustic events and determine the relationship of occurrence and peak amplitude.

To obtain large datasets, acoustic events were auto-picked by using the short- to long-term average ratio (STA/LTA) detection code from the GISMO Toolbox (Thompson & Reyes, 2019) developed in *MATLAB*. After the events were auto-picked, I applied a filter to ignore peak amplitudes under 0.0032 volts or 0.32g; therefore, values close to or under the RMS values of noise were ignored. I created a code to create the occurrence vs peak amplitude plots, which is presented in Appendix A.

Frequency Plots

I analyzed waveforms of single events using the power frequency spectrum and spectrograms. Traditionally, the frequency spectrum is calculated by the Discrete Fourier Transform (DFT), but I calculated the power spectral density estimate using the Thomson multi-taper method (The MathWorks, Inc., 2019).

Spectrograms are useful visual representations to study the evolution of frequency content with time and are calculated using the Continuous Wavelet Transform (CWT, The MathWorks, Inc., 2019). The following spectrogram representing noise has three axes (Figure 2.3): time in milliseconds on the x-axis, frequency in kHz on the y-axis log-scale, and the z-axis is acceleration (or amplitude) that is represented by colors, where brighter colors represent higher accelerations (or amplitude). The range of colors in the spectrograms are determined by taking the median of the amplitudes plus or minus the standard deviation of the CWT. Further details on the calculations or plots of the frequency spectrum or spectrograms can be found in Appendix A.

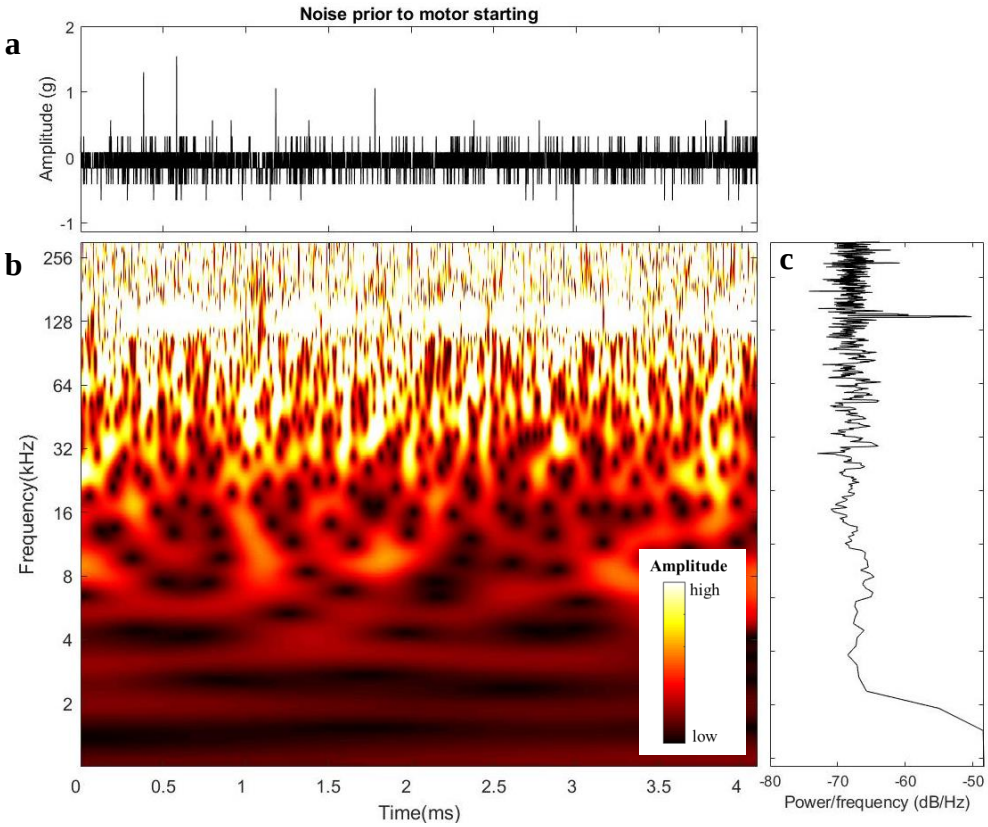

Figure 2.3 (a) Accelerogram , (b) spectrogram, and (c) power spectrum of noise prior to the motor starting. In the spectrogram (b) brighter colors represent greater acceleration at the time and frequency. The RMS value of noise is ~0.19g (or 0.0019 volts).

Chapter 3 Frequency-Magnitude Analysis of Acoustic Emissions

Background

In observational seismology, it is typical to show the magnitude-frequency relationship of earthquakes in a region (Gutenberg & Richter, 1944), which is a logarithmic scale plot of the number of earthquakes of a certain magnitude and greater. That is

$$\log_{10} N = a - bM$$

where N is the cumulative number of earthquakes with a magnitude $\geq M$, a represents the seismicity rate of the region, and b (commonly referred to as b-value) is typically close to 1. A b-value of 1 means that for a given number of magnitude 5.0 earthquakes, it is probable to have 0.1 times the number of magnitude 6.0 earthquakes and 10 times the number of magnitude 4.0 earthquakes. The variabilities in b-value have been linked to different factors such as the mechanical properties of rocks (Scholz, 1968) and stress regimes (Schorlemmer, et al., 2005).

I apply the Gutenberg-Richter (GR) relationship for acoustic events created along single-lithology and bi-material faults to explore the behavior different rock types and pairs have on acoustic event population.

Experimental Conditions

Many experiments were run using both the high velocity and slow velocity motors. It was difficult to generate acoustic emissions with the slow motor. To find the best conditions for generating acoustic emissions with the slow motor, I adjusted the normal stress, sample roughness, velocity, humidity, and experimental sample combinations. Acoustic emissions were only recorded ~20% of the time. Due to the difficulty in acquiring acoustic emissions with the

slow motor, I present and discuss two sets of experiments along all nine experimental combinations. The experimental conditions of the two sets are:

Set 1: Shear velocity of 1 mm/s, a normal stress of 0.6 to 0.7 MPa, a total slip of 0.3 m

Set 2: Shear velocity of 1 cm/s, a normal stress of 0.7 to 0.8 MPa, a total slip of 1.8 m

Due to limitations of the recording system, each set includes two recording periods: the first 8s and 14s at the start of the experiment for 1 cm/s and 1 mm/s, respectively. The second recording of acoustic emissions is at approximately two-thirds of the total slip. All experiments start with a bare surface fault, and to distinguish between the two recordings, I will use 'fresh surface' to refer to the first recording and 'worn surface' to refer to the later recording.

Observations

The recorded acoustic emissions reveal two general radiation types (Figure 3.1): (1) intense, frequent, low amplitude events referred to as 'chatter' (Figure 3.2a) which consistently appear when at least one experimental sample is sandstone and (2) distinct, high amplitude events (Figure 3.2c) observed experiments containing gabbro and/or dolomite. As a reminder, when addressing an experimental combination (i.e. GB-SS) the first lithology is recording block (i.e. GB) and the second lithology is the rotating block (i.e. SS).

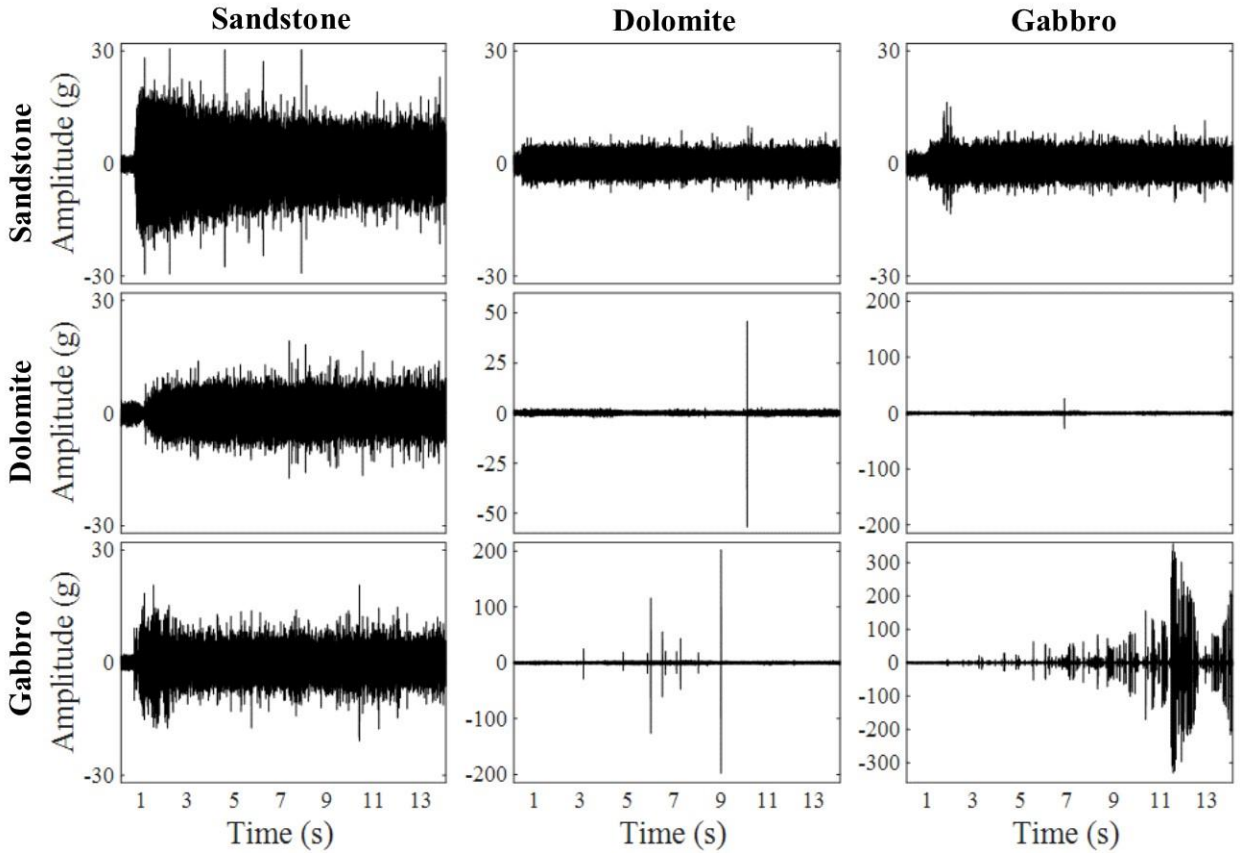

Figure 3.1 Set of raw acoustic emission data for each rock block pair sheared at 1 mm/s. The set is a matrix, where columns represent the top block and rows represent the bottom block. Acoustic emissions from experiments containing sandstone show a constant chatter, while events from dolomite and/or gabbro have individual spikes that are distinct acoustic events.

Acoustic Emissions of Sandstone Experiments

Experiments containing sandstone have acoustic emission behavior that has constant chatter during shear. The amplitude of chatter differs depending on the experimental combination (i.e. GB-SS), the recording window (i.e. fresh vs worn), and the recording block (i.e. GB or SS). To quantify the chatter intensity, I took the root mean square (RMS) of the amplitude in g (Figure 3.3). RMS values from these experiments range from 0.5 g to 3.5 g, which are greater than RMS values of the background chatter regarded as 0.19 g (Figure 2.3).

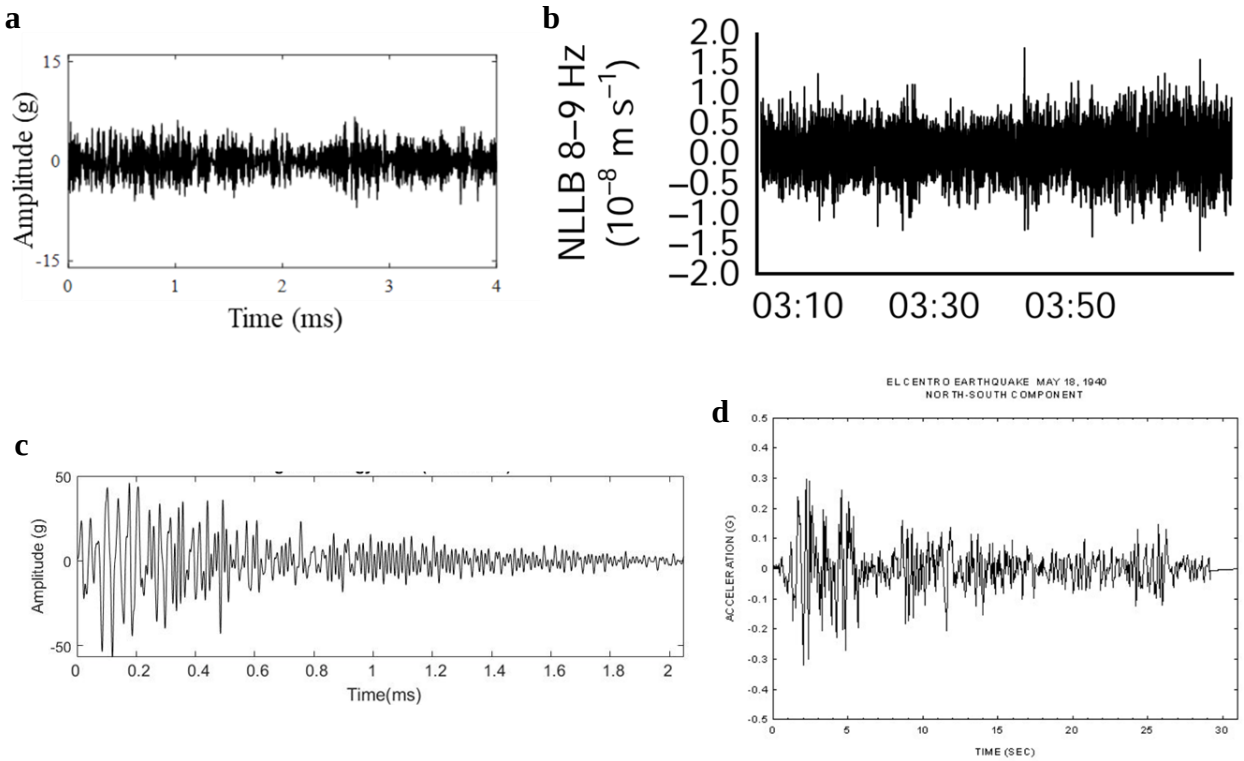

Figure 3.2 (a) Plot of acoustic emissions from sandstone-sandstone. (b) Plot of seismic tremor from the Cascadia subduction zone (Rouet-Leduc, et al., 2019). (c) Plot of acoustic emissions from dolomite-dolomite. (d) Plot of the El Centro earthquake in 1940 (Kim, et al., 2008).

Two trends emerge from the RMS value analyses (Figure 3.3): (1) On average, there is a decrease in intensity from fresh to worn fault surfaces; for example, the RMS value for SS-GB at 1 cm/s along a fresh fault surface is 3.5 g, while the RMS value for SS-GB at 1 cm/s along a worn fault surface is 2.1 g. (2) There is a greater intensity of chatter while recording acoustic emissions on the sandstone rather than through the opposing side in a bi-material setup. For example, the RMS value for SS-DOL at 1 mm/s along a fresh fault surface is 1.4 g, while the RMS value for DOL-SS at 1 mm/s along a fresh fault surface is 0.9 g.

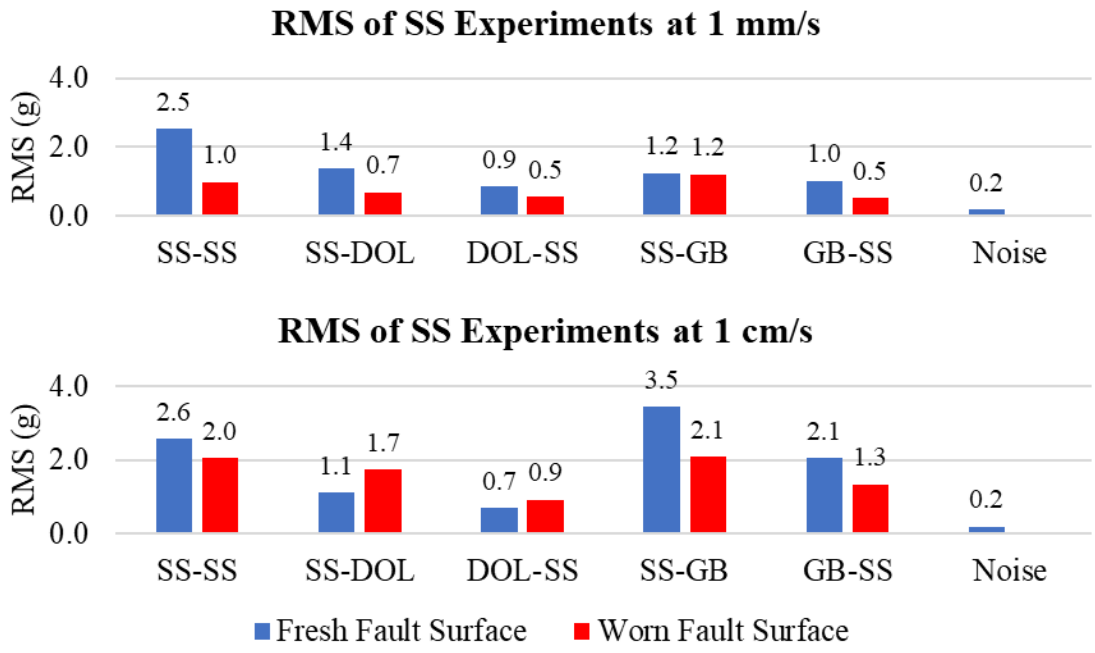

Figure 3.3 Root mean square (RMS) values for experiments containing sandstone from experiments sheared at 1 mm/s and 1 cm/s along fresh and worn fault surfaces.

Acoustic Emissions of Gabbro and Dolomite Experiments

Acoustic emissions from experiments composed of gabbro and/or dolomite have distinct impulsive events that resemble records of natural earthquakes (Figure 3.2d). The Gutenberg-Richter (GR) relationships of peak amplitude (PA) in the present experiments are presented in Figure 3.5 where N is the number of events that have a peak amplitude ≥ PA in volts.

I have shown this relationship for the x, y, and z spatial directions from each accelerometer along a fresh fault surface sheared at 1 mm/s (Figure 3.4). When comparing the spatial directions with each other, they tend to show similar relationships with each other, which is an expected result for same events in different dimensions. The GR plots for 1 mm/s along a worn surface, 1 cm/s along a fresh surface, and 1 cm/s along a worn surface are shown in Appendix B (Figures B.5, B.6, and B.7, respectively).

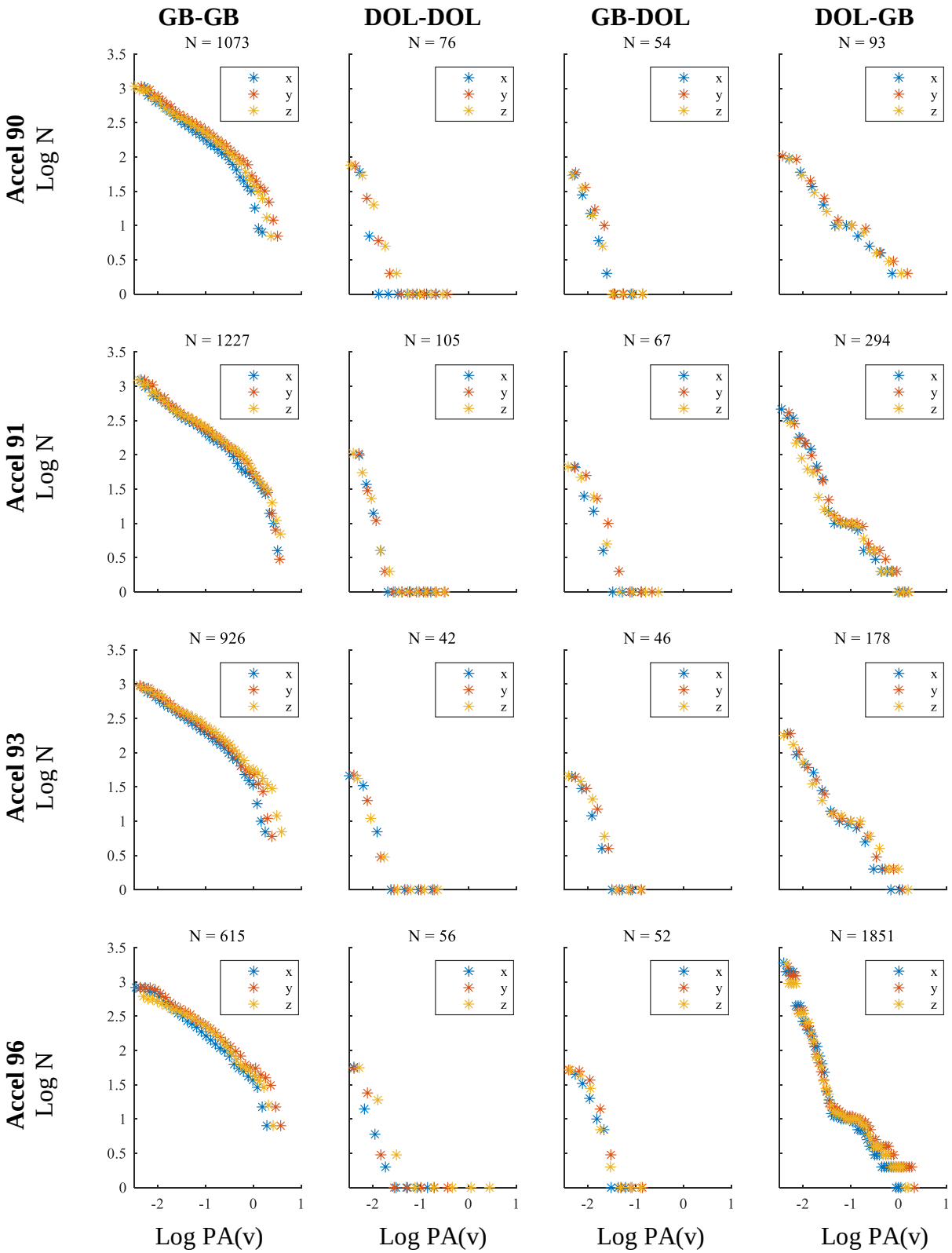

Figure 3.4 The GR plot of peak amplitude (PA) plots showing the x, y, z spatial directions for the 4 accelerometers and the 4 experimental combinations sheared along fresh fault surfaces at 1 mm/s.

I compare the relationship between the four accelerometers by taking the geometric mean of the peak amplitude of the 3 spatial directions ($\sqrt[3]{X \times Y \times Z}$). This is done to remove possible bias that could arise from various angles events can take from source to accelerometer. This was done for all for datasets for fresh and worn fault surfaces sheared at 1 mm/s and 1 cm/s (Figures 3.5, 3.6, 3.7, and 3.8).

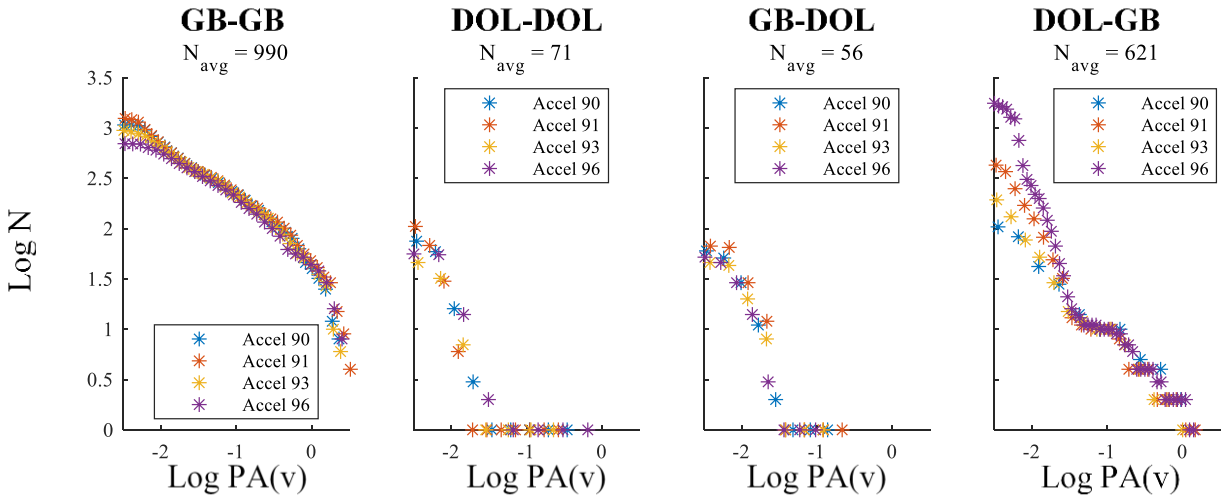

Figure 3.5 The GR plot of peak amplitude (PA) plots showing all 4 accelerometers after taking the geometric mean of x, y, and z for the 4 experimental combinations sheared along fresh fault surfaces at 1 mm/s. N_{avg} shows the average number of events found by the auto-picking.

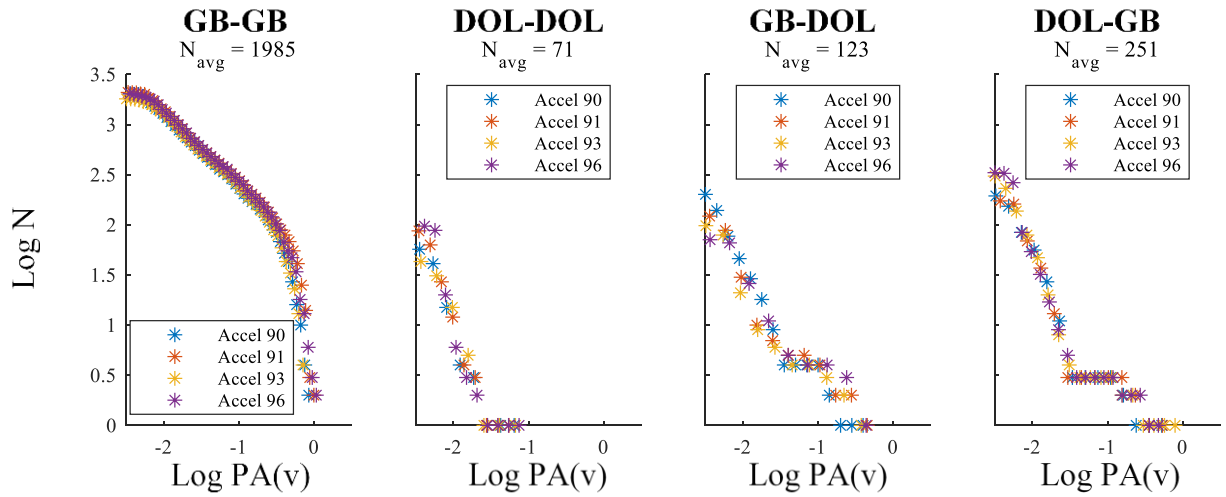

Figure 3.6 The GR plot of peak amplitude (PA) plots showing all 4 accelerometers after taking the geometric mean of x, y, and z for the 4 experimental combinations sheared along worn fault surfaces at 1 mm/s. N_{avg} shows the average number of events found by the auto-picking.

I took the total number of events from the four accelerometers and averaged them to compare the experimental pairs (i.e. Figure 3.7). In terms of those numbers, GB-GB has the largest number of events, while DOL-DOL typically has the least. The two bi-material faults of GB and DOL have an intermediate number of events, typically being closer to the range of DOL-DOL. Only GB-DOL from the fresh fault surface sheared at 1 mm/s (Figure 3.5) does not follow this trend and has a smaller number of events than DOL-DOL.

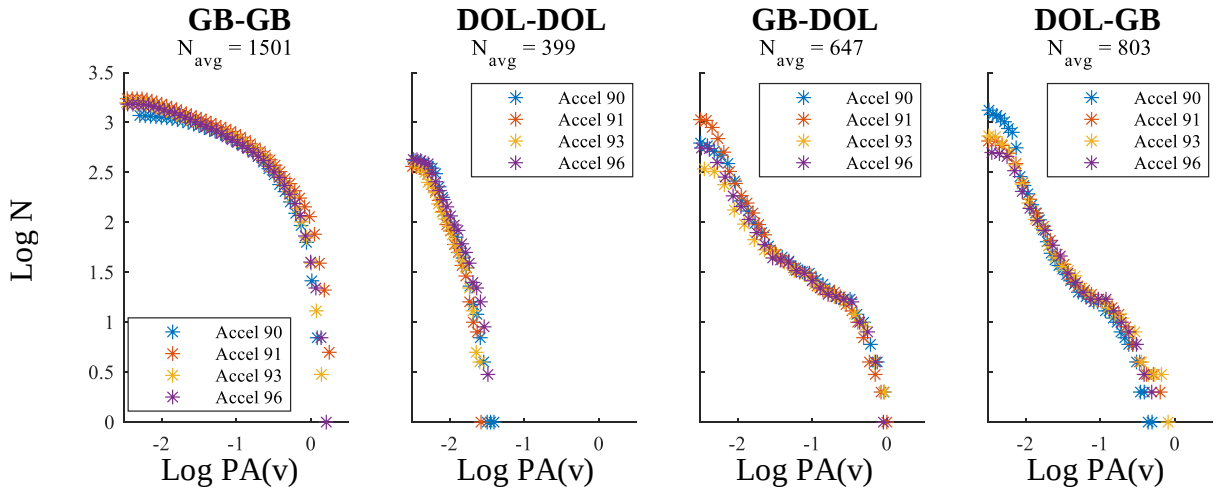

Figure 3.7 The GR plot of peak amplitude (PA) plots showing all 4 accelerometers after taking the geometric mean of x, y, and z for the 4 experimental combinations sheared along fresh fault surfaces at 1 cm/s. N_{avg} shows the average number of events found by the auto-picking.

When comparing different accelerometers with each other for a given rock-block pair there are slight differences (i.e. DOL-GB in Figure 3.5); this is most likely an artifact of the auto-picking, where smaller events closer to one accelerometer is easier to detect. For GB-GB and DOL-DOL in all four sets, the 4 accelerometers tend to agree with each other (Figure 3.7). Typically, the biggest difference is found in GB-DOL and DOL-GB for events less than Log PA(v) of -2; these differences is most likely due to smaller events being harder to detect at different distances, a product of the accelerometers being spaced around the samples.

Furthermore, for a given experimental pair the relationship between occurrence and peak amplitude of the events remains similar between different accelerometers.

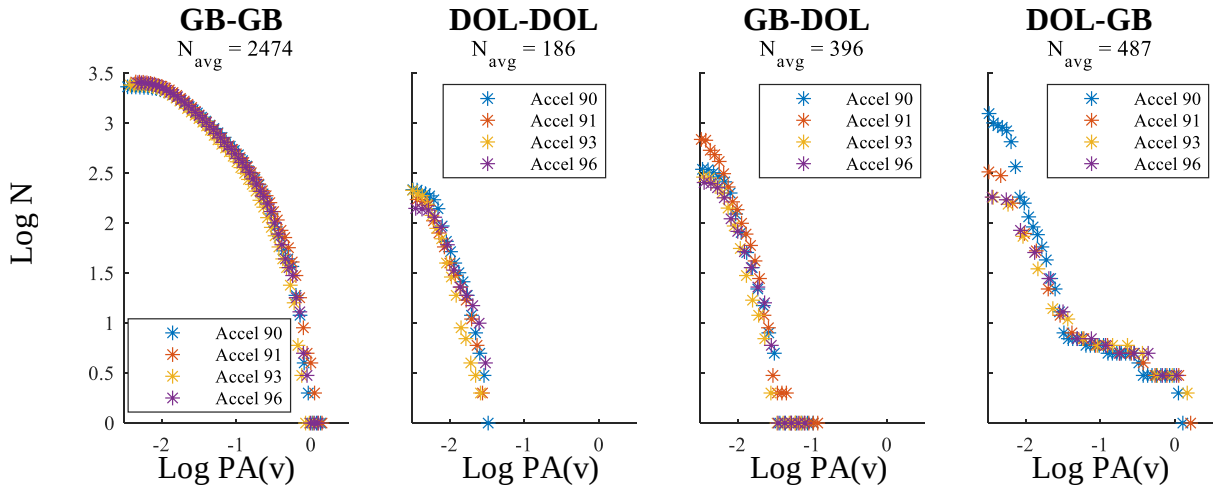

Figure 3.8 The GR plot of peak amplitude (PA) plots showing all 4 accelerometers after taking the geometric mean of x, y, and z for the 4 experimental combinations sheared along worn fault surfaces at 1 cm/s. N_{avg} shows the average number of events found by the auto-picking.

To remove the possible bias of the source of acoustic emissions, I combined the data from the four accelerometers. In this case, I did not take the average of the four accelerometers, rather the data from the four accelerometers are compiled into one dataset. This was done for all experimental pairs (Figures 3.9, 3.10, 3.11, and 3.12).

The GR relationship in single lithology faults show that while acoustic events in DOL-DOL are typically no larger than 0.03 volts, the events in GB-GB have a range up to 3.2 volts, which is 100 times the typical size of events in DOL-DOL (for 1 mm/s, Figure 3.9 and for 1 cm/s, Figure 3.11).

The GR relationship in bi-material faults show similar behaviors with each other (for 1 mm/s, Figures 3.10 and for 1 cm/s, Figure 3.12). This behavior was expected for the same experimental pairs, since the mechanical properties of the two lithologies do not change and does not depend on the recording block. The GR relationship shows a bimodal distribution of acoustic

events. That is, there are two trends that emerge on the GR plots, the first trend ranges from -2.5 to -1.5 on the x-axis, followed by a plateau between -1.5 to -1.0, then the second trend has values greater than -1.0 on the x-axis.

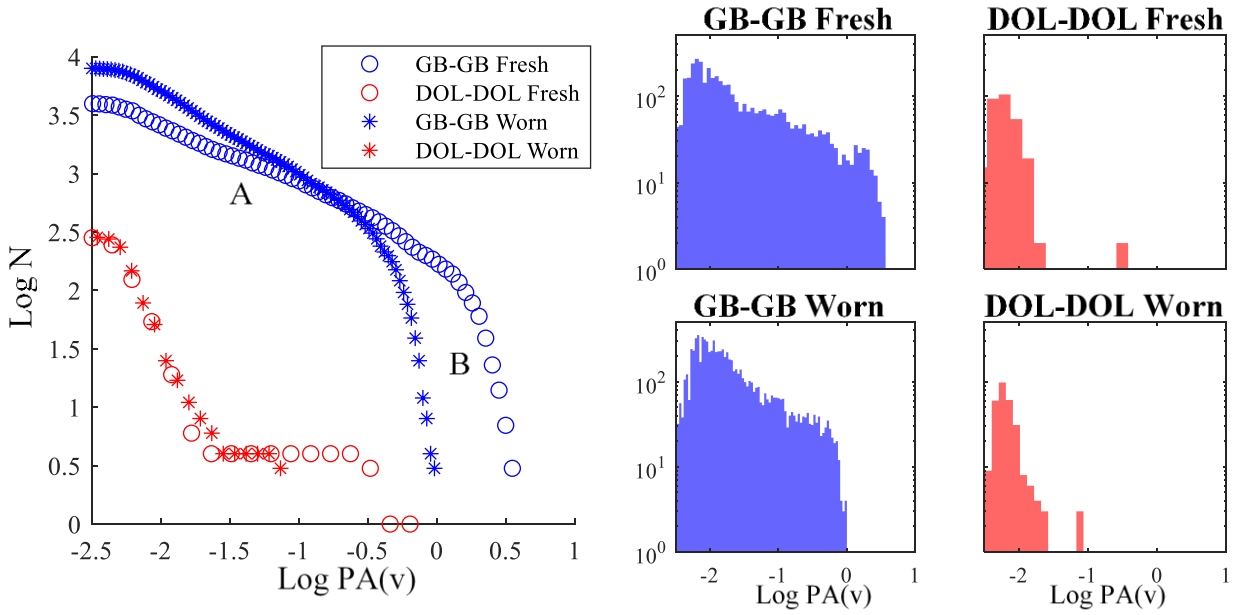

Figure 3.9 The GR plot of peak amplitude (PA) relationship of acoustic events in single lithology faults sheared at 1 mm/s along fresh and worn fault surfaces, along with their corresponding histograms. Two linear relationships are seen in GB-GB, slope A and slope B; their b-values are listed in Table 2.

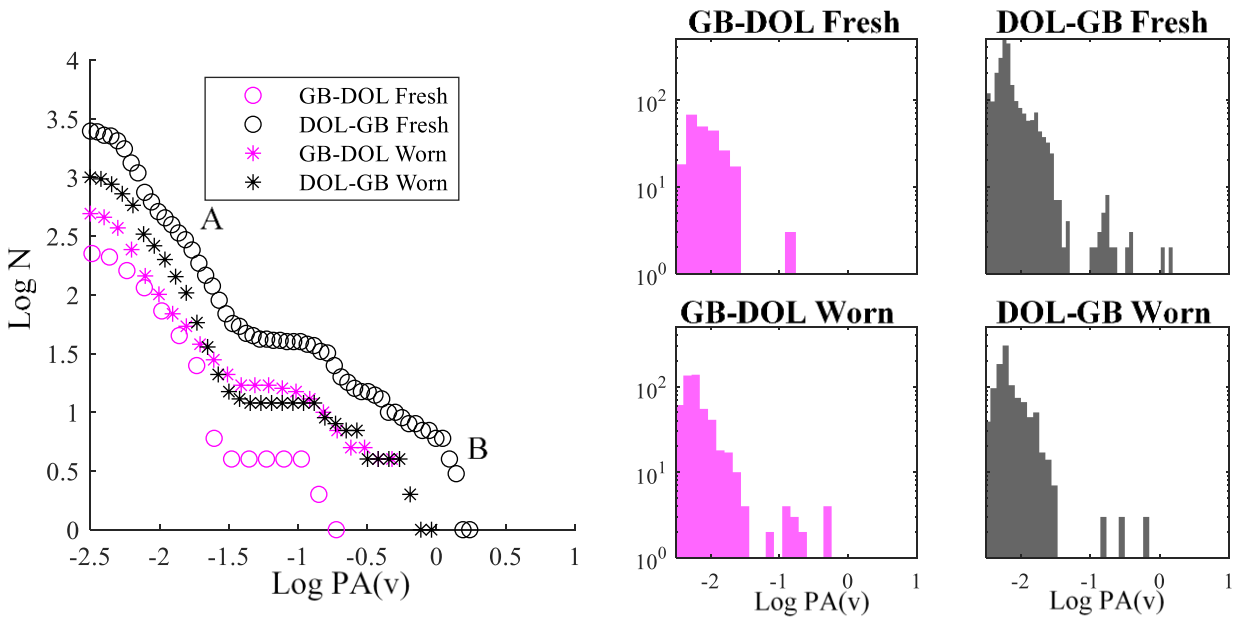

Figure 3.10 The GR plot of peak amplitude (PA) relationship of acoustic events in bi-material faults sheared at 1 mm/s along fresh and worn fault surfaces, along with their corresponding histograms. A bimodal distribution is seen in all four cases, slope A and slope B represent those two trends; their b-values are listed in Table 2.

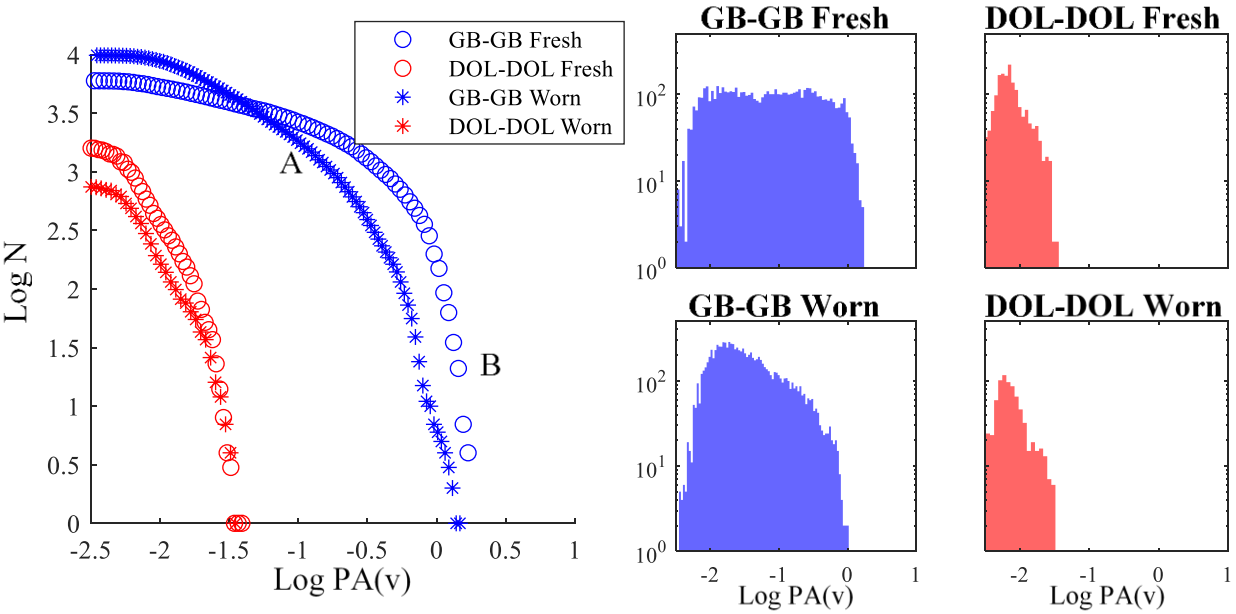

Figure 3.11 The GR plot of peak amplitude (PA) relationship of acoustic events in single lithology faults sheared at 1 cm/s along fresh and worn fault surfaces, along with their corresponding histograms. Two linear relationships are seen in GB-GB, slope A and slope B; their b-values are listed in Table 2.

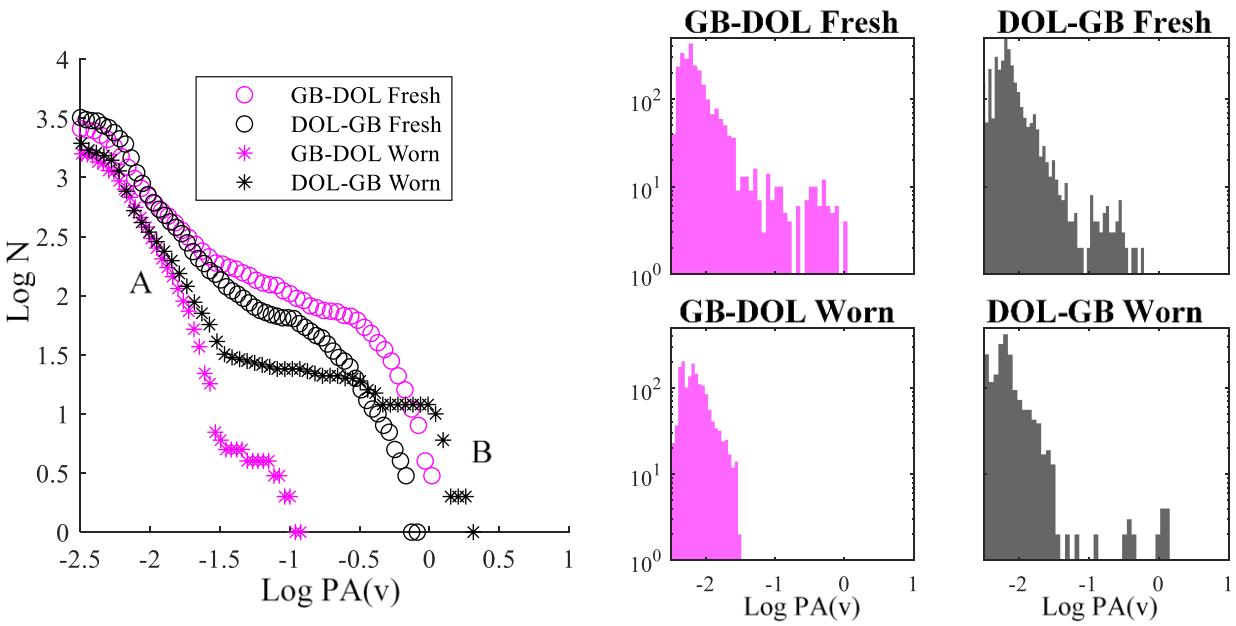

Figure 3.12 The GR plot of peak amplitude (PA) relationship of acoustic events in bi-material faults sheared at 1 cm/s along fresh and worn fault surfaces, along with their corresponding histograms. A bimodal distribution is seen in all four cases, slope A and slope B represent those two trends; their b-values are listed in Table 2.

Table 3.1 b-values of different experimental combinations

	1 mm/s		1 cm/s	
Single Lithology Faults	Fresh	Worn	Fresh	Worn
GB-GB Part A	0.5	0.7	0.4	0.7
GB-GB Part B	3.7	5.0	4.4	4.0
DOL-DOL	2.2	2.2	1.3	1.1
Bi-material Faults				
	1 mm/s		1 cm/s	
	Fresh	Worn	Fresh	Worn
GB-DOL Part A	1.8	1.5	0.9	2.4
GB-DOL Part B	1.7	0.8	2.3	2.5
DOL-GB Part A	1.7	1.7	1.3	1.8
DOL-GB Part B	1.1	0.9	1.9	1.4

Note: b-values correspond to N vs PA relationships seen in Figures 3.11, 3.12, 3.13, and 3.14

The calculated b-values of GR plots for all rock block combinations are displayed in Table 3.1. The b-values are the slopes of the linear regression of the data in the N vs PA plots

and they show the number of small events per large event. A small b-value (or a shallow trendline) indicated few small events per large event, while for large b-values it would be expected to have more small events per large event.

DOL-DOL experiments has b-values that range from 1.1 to 2.2. GB-GB experiments show two trends; the first trend is between -2.5 and -0.5 on the x-axis (labeled as Part A in Figures 3.9 and 3.11), while the second trend is -0.5 and greater on the x-axis (Part B in Figures 3.9 and 3.11). Trendlines for part A are shallow and have b-values that range from 0.4 to 0.7, while Part B the trendlines are steep with b-values ranging from 3.7 to 5.0.

For the bi-material faults, the bimodal distribution is visualized by the plateau in the N vs PA plots, with two b-values before and after the plateau. The first b-value is determined from the data trend before the plateau (Part A in Figures 3.10 and 3.12), while the second b-value is determined from the data trend after the plateau (Part B in Figures 3.10 and 3.12). For the first trend (Part A) in both GB-DOL and DOL-GB the b-values range from 0.9 to 2.4, while the second trend (Part B) has b-values the range from 0.9 to 2.5.

Discussion

Experiments with Sandstone

The presence of sandstone in the experiments strongly affect the characteristics of acoustic emissions. The behavior seen in the sandstone is most likely due to individual sand grains breaking from cement followed by grain crushing with further shear displacement. The chatter seen in experiments containing sandstone resembles closely to low amplitude tremor seen from natural fault zones (e.g. Figure 3.2c; Rouet-Leduc, et al., 2019). Tremor is thought to indicate continuous slow slip along the fault; therefore, asperity locking for long periods and then release of large events are not expected.

The differences in RMS values of the acoustic emissions are due to fault conditioning and accelerometer location (i.e. on gabbro, dolomite, or sandstone). The average decrease in RMS values from fresh to worn fault surfaces is likely due to fault surface smoothening and gouge formation. Furthermore, the difference in RMS values when comparing SS-DOL vs DOL-SS and SS-GB vs GB-SS is due to accelerometer location. As the acoustic event propagates from the failing sand grains, there is an impedance contrast at the fault contact due to the two lithologies. Since gabbro and dolomite have a higher impedance, a portion of the acoustic emission energy is going to reflect rather than be transmitted through the fault contact, resulting in lower amplitude chatter when recording on gabbro or dolomite rather than sandstone.

Experiments Containing Gabbro and/or Dolomite

Unlike experiments that contain sandstone, where the presence of sandstone strongly affects the behavior of the acoustic emissions, experiments that are composed of gabbro and dolomite have an intermediate total number of events. For example, the number of events in GB-GB is greater than all other experimental combinations, while DOL-DOL has the least. The bi-material faults (GB-DOL and DOL-GB) have an intermediate number of events between the two end members of GB-GB and DOL-DOL.

The GR relationship of the bi-material faults seems to incorporate both single-lithology faults. Besides a few outliers, DOL-DOL does not have events greater than 0.03 volts, while GB-GB has events up to 3.2 volts. The event size threshold seen in DOL-DOL is most likely due to the strength of the rock not allowing large events to occur. GB-GB, for instance, has greater strength allowing for larger events to occur.

The fact that both GB-DOL and DOL-GB have large events show that GB is contributing to the acoustic emission behavior. This is important because the behavior of the acoustic

emissions does not strictly follow the weaker rock, rather the mechanical properties of both rock-blocks are contributing to the acoustic emission characteristics, and therefore, contribute to the fault mechanics. These results are important to earthquake physics in terms of asperity breaking and gouge formation along the contact of the fault. The b-value is an important seismological parameter in terms of seismic hazards (Gutenberg & Richter, 1944) and these results show a dependence b-values have on the contrasting materials of a bi-material fault. Characterizing b-values as it relates to contrasting material along fault contacts may give better estimates to varying b-values found for natural earthquakes, and therefore, better estimates for seismic hazards.

Summary

To study the behavior of bi-material faults, I ran experiments in a rotary shear apparatus by shearing rock-blocks of different material and mechanical properties (i.e. sandstone, dolomite, and gabbro). The recorded acoustic emissions along experimental faults that contain sandstone have tremor like behavior, while acoustic emissions along faults composed of gabbro and/or dolomite create distinct acoustic events closely resembling natural earthquakes (Figure 3.2d).

The presence of sandstone tends to strongly affect the behavior of acoustic emissions, while the mechanical properties of the opposing experimental samples do not play a strong role in the acoustic emission characteristics. This is not the case in experiments containing only dolomite and gabbro. The bi-material faults of gabbro and dolomite seems to mimic the behavior of both the single lithology faults in both the total number of acoustic events and the relationship between occurrence and peak amplitude. This implies that faults do not necessarily follow the behavior of the compliant rock, but the mechanical properties of both rocks affect the behavior of the fault.

Chapter 4 Frequency Spectrum Analysis

Background

Three major factors that contribute to ground shaking during an earthquake (Kentucky Geological Survey, 2012; Figure 4.1A): (1) Source effects, such as fault geometry, size and the direction of rupture, and slip velocity; (2) wave propagation, such as the effects of lithology and its effects on transmitting energy, wave scattering, and seismic velocities; and (3) local site conditions, which depends on the location of seismic stations, such as soil composition and liquid saturation.

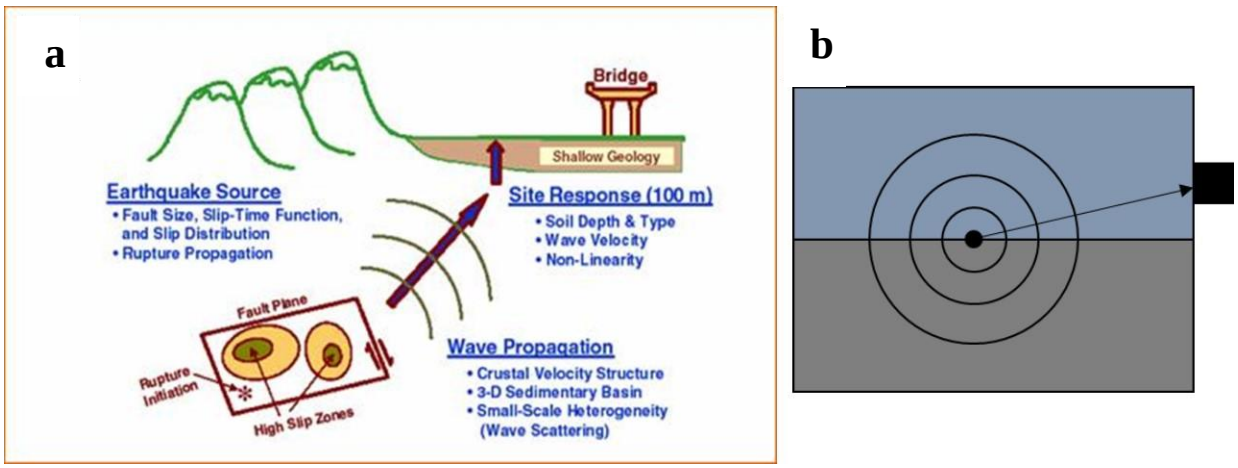

Figure 4.1 (a) Illustration of contributing factors in a seismogram (modified from Kentucky Geological Survey, 2012) and (b) illustration of a cross-section showing the contributing factors seen in the acoustic emissions from the present experiments.

Similarly, in the present experiments there are multiple factors that contribute to the accelerograms of acoustic events (Figure 4.1B): (1) source effects, affected by the lithologies (i.e. dolomite-gabbro) in contact by the experimental fault; (2) wave propagation path, the effect of the samples as waves propagate through the rock before reaching the accelerometers (i.e. dolomite); and (3) local site conditions, epoxy and accelerometer mounts. I use the following equation to illustrate their effects in the frequency domain:

$$A(w) = S(w) + P(w) + L(w),$$

where w is frequency, A is amplitude, S is source effect, P is wave propagation path effect, and L is the local site condition effect of the accelerometers. Since epoxy and accelerometers mounts are similar in the experiments, I ignore local site conditions as a major contributing factor in these experiments.

Results and Discussion

An important reminder is that I will list 'recording block – rotating block' to refer to an experiment where the accelerometers are attached to the recording block (i.e. gabbro-sandstone, the accelerometers are on gabbro). For repeatability sake, I compared two events of similar peak amplitude from a GB-GB experiments (Figure 4.2). The two waveforms show similar spectrograms and frequency content, which is important for later comparisons.

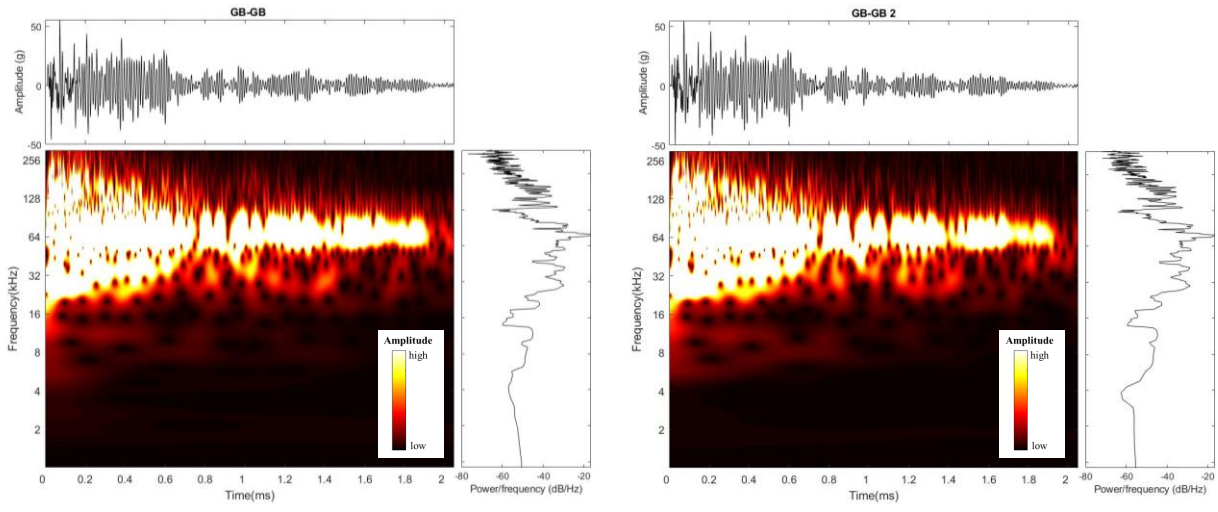

Figure 4.2 Comparing the waveforms of two separate events of similar peak amplitude from a GB-GB experiment.

<u>The Effect of Wave Propagation Path</u>

I compare two events that occurred along bimaterial faults using the same lithologies, such that the fault contact has the same lithological composition. The difference between the two events is that the events are recorded from accelerometers that are attached on different lithologies. Furthermore, comparing two events that have the same experimental combination

with similar peak amplitude and recorded on opposing sides of a bi-material, reveals the difference in the wave propagation path.

I compare two events from experiments containing sandstone (SS) and gabbro (GB) in the y transverse direction. One event was recorded with an accelerometer attached to the SS with a peak amplitude of 18g (Figure 4.3), while the other event was recorded with an accelerometer attached to the GB with a peak amplitude of 16g (Figure 4.4). A common feature in all events is the high amplitude at ~80 kHz; this feature is a known accelerometer response of the accelerometers.

The spectrograms of both events have ranges of interest that are circled for comparison. The event through the sandstone (Figure 4.3), has high energy at frequencies of 10 to 30 kHz and low energy at frequencies of 100 to 200 kHz. The dominant frequency of this event is approximately 19 kHz. In contrast, the event through the gabbro (Figure 4.4), has low energy at 10 to 30 kHz and high energy at frequencies between 100 to 200 kHz. The dominant frequency for this event is approximately 41 kHz.

Since the event through sandstone at low frequencies has higher energy and at high frequencies has lower energy when comparing it to the event through the gabbro, I attribute this difference to the wave propagation path. As the event travels through the sandstone higher frequencies are being attenuated, most likely due to wave scattering (Shapiro & Kneib, 1993) at grain to grain contacts due to the poorly cemented rock. The event through the gabbro does not have the same effect due to the homogeneity of the crystalline rock.

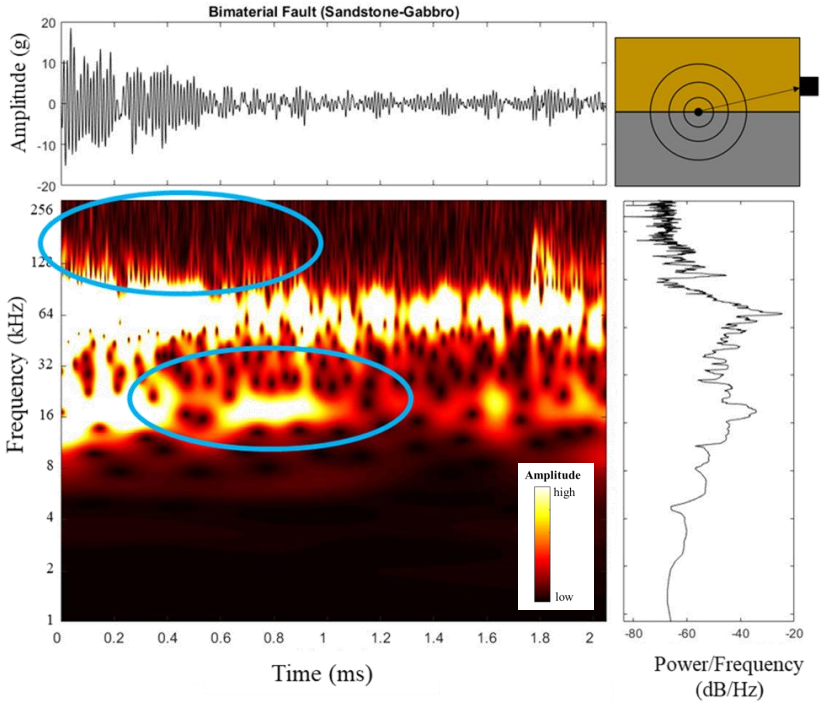

Figure 4.3 Accelerogram, spectrogram, and power spectrum of a single event in a sandstone-gabbro experiment. The acoustic event is 2ms in duration with a peak amplitude of 18g. Besides the machine response at ~80kHz, the dominant frequency is ~19kHz. This event is compared with the event in Figure 4.4.

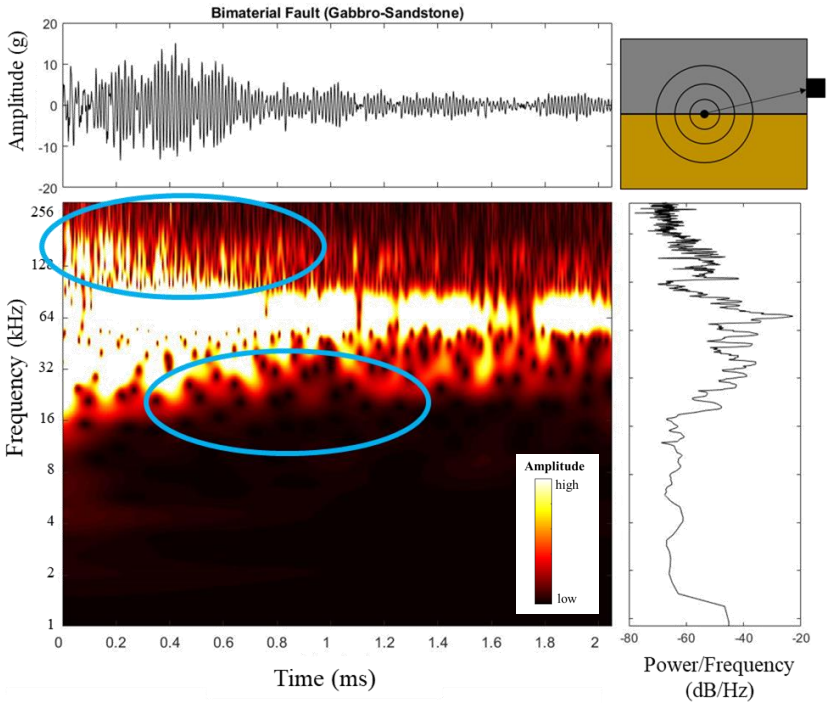

Figure 4.4 Accelerogram, spectrogram, and power spectrum of a single event in a gabbro-sandstone experiment. The acoustic event is 2ms in duration with a peak amplitude of 16g. Besides the machine response at ~80 kHz, the dominant frequency is ~41 kHz. This event is compared with the event in Figure 4.3.

Source Effects

A similar comparison can be made concerning source effects. This is done by comparing two events, with similar peak amplitude, from two different experimental pairs, such as a single lithology fault (i.e. dolomite-dolomite) and a bi-material fault (i.e. dolomite-gabbro) but keeping the recording block the same (i.e. dolomite). This way the wave propagation path stays the same but the composition of the fault contact changes, hence the source effects.

For this comparison, I selected one event from a dolomite-dolomite experiment with a peak amplitude of 46g (Figure 4.5) and the other event is from a dolomite-gabbro experiment with a peak amplitude of 44g (Figure 4.6). The event in dolomite-dolomite has high energy at frequencies between 10 and 60 kHz and low energy at frequencies above 100 kHz. In contrast, the event from the dolomite-gabbro experiment has more energy at higher frequencies above 100 kHz compared to the lower frequencies between 10 and 60 kHz. The differences in frequency content is seen in the waveforms in the accelerograms; the peaks and troughs of the event form dolomite-dolomite is easily seen compared to the event form dolomite-gabbro.

The high frequency content in both events indicates impulsive asperity failure. The higher frequency content in the dolomite-gabbro event compared to the event from dolomite-dolomite indicates that the gabbro is playing a part in the breaking of asperity contacts. Furthermore, the strength of the gabbro causes the breaking of the asperity to be more impulsive compared to the dolomite-dolomite event. Making comparisons of acoustic emissions from different experiments have been made by McLaskey and Glaser (2011), who compared stick-slips created by two experiments of PMMA against PMMA and granite against granite (Figure A.3). Their conclusion was that the stick-slips in the granite were impulsive, earthquake like, while stick slips in the PMMA more closely resembled tremor-like behavior.

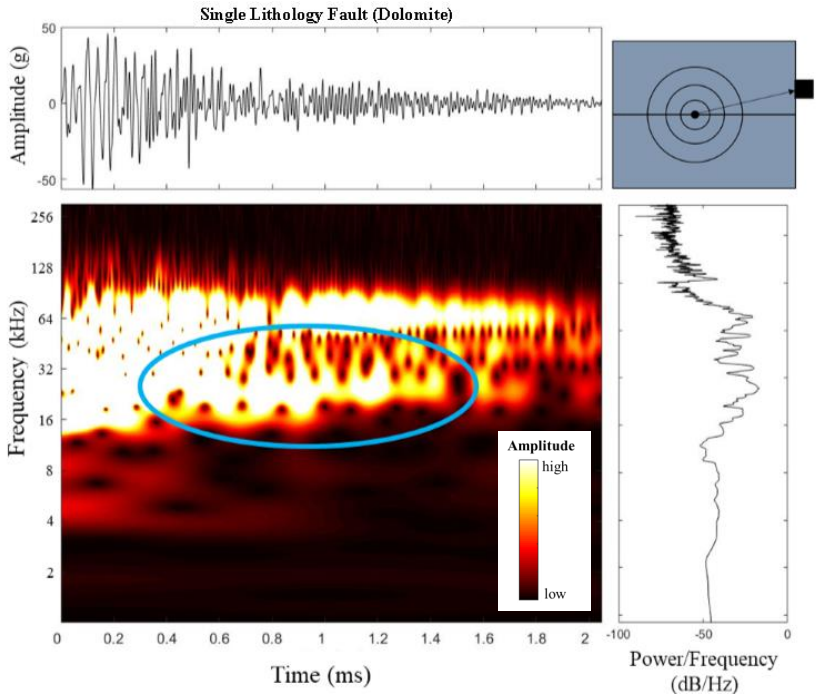

Figure 4.5 Accelerogram, spectrogram, and power spectrum of a single event in a dolomite-dolomite experiment. The acoustic event is 2ms in duration with a peak amplitude of 46g. The frequency band at ~80 kHz is due to machine response and is ignored for comparisons. This event is compared with the event in Figure 4.6.

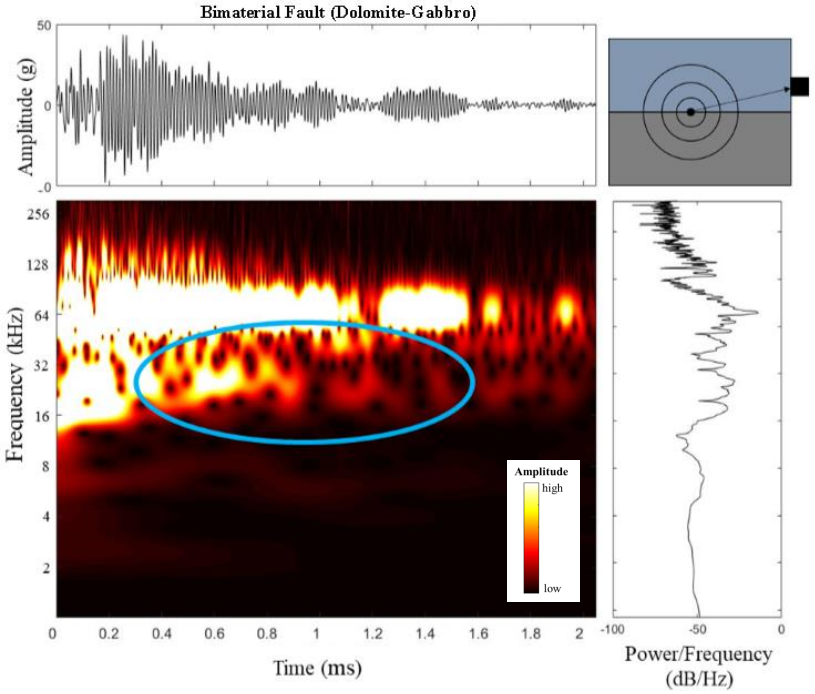

Figure 4.6 Accelerogram, spectrogram, and power spectrum of a single event in a dolomite-gabbro experiment. The acoustic event is 2ms in duration with a peak amplitude of 44g. The frequency band at ~80 kHz is due to machine response and is ignored for comparisons. This event is compared with the event in Figure 4.5.

Summary

I use frequency spectrum content and spectrograms to study the behavior of single acoustic events created along experimental faults to study source and ray path characteristics as it relates to different experimental pairs. To study ray path characteristics, I compare two events that were created along the same experimental pairs but recorded on opposite sides of the fault. For example, I compared two events created along a SS and GB contact, when recording the acoustic event on the SS rather than the GB there are lower frequency content. This suggests that the higher frequencies have been attenuated out, most likely by wave scattering. Furthermore, to study source characteristics, I compare two events created along different experimental pairs but recorded the event on the same experimental sample. For example, I compared two events recorded through dolomite, but one event was created by DOL-DOL and the other was created by DOL-GB. The difference in frequency content is due to source effects; the DOL-GB had a higher frequency content compared to DOL-DOL, which suggest that the asperity break in DOL-GB was more impulsive with gouge formation.

Chapter 5 Final Summary

Experimental Summary

Bi-material faults have two materials with different mechanical properties juxtaposed by a fault. Natural bi-material faults are found along large displacement faults and are observed world-wide. There have been many studies of natural bi-material faults, theoretical bi-material faults, and experimental bi-material faults using non-geological materials. I conducted experiments, by shearing rock blocks of either sandstone, dolomite, or gabbro to study the acoustic emissions that radiate from the experimental fault.

I have shown that acoustic emissions along faults composed of sandstone have tremor-like behavior likely caused by individual sand grains breaking, while acoustic emissions along faults composed of gabbro and dolomite have many impulsive events resembling natural earthquakes. The GR plots of peak amplitude of acoustic events from the bi-material faults of gabbro and dolomite show that fault behavior does not follow the behavior of the compliant rock. In fact, the bi-material faults mimics both the behaviors of the single lithology faults of gabbro and dolomite.

Furthermore, frequency spectrum data revealed that the differences in seismic radiation are due to rupture and ray path characteristics. For example, for an experimental fault composed of gabbro and sandstone, the recorded events on the more compliant side (sandstone) of the fault have low amplitudes (low accelerations) at higher frequencies. I deduced that the ray path, which is controlled by the rock block properties, is responsible for this difference and is likely due to high frequency data being scatter at grain to grain contacts. I also observed that while keeping the ray path constant (i.e. dolomite) but changing the other fault block, to either gabbro or

dolomite, indicated differences in the frequency content, this time due to rupture characteristics of the laboratory earthquakes.

These experiments show the distinct dependence of seismic radiation on the mechanical properties of the three lithologies. Furthermore, they indicate that bimaterial faults exhibit strong control on the mechanisms of fault rupture and the frequency content of seismic radiation.

The main takeaways are:

1. Bi-material faults do not necessarily follow the behavior of the weaker material, rather bi-material faults have intermediate behaviors, where the single-material faults act as end members.
2. While looking at the frequency spectrum of an acoustic event and considering its ray path, experimental faults containing stiffer rocks tend to transmit higher frequencies, while more compliant rocks, such as sandstone, tend attenuate out the higher frequencies.
3. Concerning the frequency spectrum of an acoustic event and considering source effects, experimental faults containing stiffer rocks (i.e. gabbro) tend to have impulse events compared to experimental faults that contain compliant rocks (i.e. dolomite).

Implications

In terms of natural earthquakes, this research has important implications on seismic hazards. Allam et al. (2014) showed that the contrast in seismic velocities along the bimaterial contact of the Hayward fault has a preferred rupture direction to the SE, an important note since dense populations are located on the opposite side of the fault. In addition to velocity contrasts,

the present results show that the contrast in mechanical properties along a bi-material fault, not only affects rupture directivity, but may affect earthquake magnitude.

Furthermore, the b-value is an important seismological parameter in terms of seismic hazards; b-values may vary depending on depth (Mori & Abercrombie, 1997), the focal mechanism (Schorlemmer, et al., 2005), and the mechanical properties of rocks (Scholz, 1968) of a fault. Current results show that b-values are dependent on the contrast in mechanical properties along a bi-material fault; thus, it is important to characterize b-values along different segments of a large fault where contrasting mechanical properties are in contact. This would give better b-value estimates for natural earthquakes, and therefore, give better estimates for seismic hazards.

References

Allam, A. A., Ben-Zion, Y. & Peng, Z., 2014. Seismic Imaging of a Bimaterial Interface Along the Hayward Fault, CA, with Fault Zone Head Waves and Direct P Arrivals. *Pure and Applied Geophysics,* Volume 171, pp. 2993-2011.

Ampuero, J.-P. & Ben-Zion, Y., 2008. Cracks, pulses and macroscopic asymmetry of dynamic rupture on a bimaterial interface with velocity-weakening friction. *Geophysical Journal International,* Volume 173, pp. 674-692.

Andrews, D. J. & Ben-Zion, Y., 1997. Wrinkle-like slip pulse on a fault between different materials. *Journal of Geophysical Research,* 102(B1), pp. 553-571.

Anooshehpoor, A. & Brune, J. N., 1999. Wrinkle-like Weertman pulse at the interface between two blocks of foam rubber with different velocities. *Geophysical Research Letters,* 26(13), pp. 2025-2028.

Ben-Zion, 2002. Appendix 2, Key Formulas in Earthquake Seismology. In: W. H. K. Lee, ed. *International Handbook of Earthquake and Engineering Seismology.* Amsterdam, Boston: Academic Press, p. 18571875.

Boneh, Y., Sagy, A. & Reches, Z., 2013. Frictional strength and wear-rate of carbonate faults during high-velocity, steady-state sliding. *Earth and Planetary Science Letters,* Volume 381, pp. 127-137.

Brietske, G. B., Cochard, A. & Igel, H., 2007. Dynamic rupture along bimaterial interfaces in 3D. *Geophysical Research Letters,* Volume 34, p. L11305.

Brietzke, G. B., Cochard, A. & Igel, H., 2009. Importance of bimaterial interfaces for earthquake dynamics and strong ground motion. *Geophysical Journal International,* Volume 178, pp. 921-938.

Bulut, F., Ben-Zion, Y. & Bohnhoff, M., 2012. Evidence for a bimaterial interface along the Mudurnu segment of the North Anatolian Fault Zone from polarization analysis of P waves. *Earth and Planetary Science Letters,* Volume 327, pp. 17-22.

Chester, J. S., Chester, F. M. & Kronenberg, A. K., 2005. Fracture surface energy of the Punchbowl fault, San Andreas System. *Nature Letters,* Volume 437, pp. 113-136.

Coldspring USA, 2019. *Products, Colors, & Finishes.* [Online]
Available at: https://www.coldspringusa.com/building-materials/products-colors-and-finishes/
[Accessed 26 April 2019].

Dibblee, T. W. & Minch, J. A., 2002. Geologic map of the Mount San Antonio quadrangle, Los Angeles and Sand Bernardino Counties, California. *U.S. Geological Survey.*

Dor, O., Rockwell, T. K. & Ben-Zion, Y., 2006. Geological Observations of Damage Azymmetry in the Structure of the San Jacinto, San Andreas and Punchbowl Faults in Southern California: A Possible Indicator for Preffered Rupture Propagation Direction. *Pure and Applied Geophysics,* Volume 163, pp. 301-349.

Gutenberg, B. & Richter, C. F., 1944. Frequency of earthquakes in California. *Bulletin of the Seismological Society of America,* Volume 34, pp. 185-188.

Kentucky Geological Survey, 2012. *Earthquake Hazards and Risk, ,* s.l.: University of Kentucky.

Kim, Y., Langari , R. & Hurlebaus, S., 2008. *Supervisory semiactive nonlinear control of a building-magnetorheological damper system.* s.l., American Control Conference.

Langer, S., Weatherley, D., Olsen-Kettle, L. & Finzi, Y., 2013. Stress heterogeneities in earthquake rupture experiments with material contrasts. *Journal of the Mechanics and Physics of Solids,* Volume 61, pp. 742-761.

Lykotrafitis , G. & Rosakis, A. J., 2006. Dynamic sliding of frictionally held bimaterial interfaces subjected to impact shear loading. *Proceedings: Mathematical, Physical and Engineering Sciences,* 462(2074), pp. 2997-3026.

Ma, S. & Beroza, G. C., 2008. Rupture Dynamics on a Bimaterial Interface for Dipping Faults. *Bulletin of the Seismological Society of America,* 98(4), pp. 1642-1658.

Mattaboni, P. & Schreiber, E., 1967. Method of Pulse Transmission Measurements for Determining Sound Velocities. *Journal of Geophysical Research,* 72(20), pp. 5160-5163.

McLaskey, G. C. & Glaser, S. D., 2011. Micromechanics of asperity rupture during laboratory stick slip experiments. *Geophysical Research Letters,* Volume 38, p. L12302.

Moore, D. E., Lockner, D. A. & Ponce, D. A., 2010. *Anomalously low strength of serpentinite sheared against granite and implications for creep on the Hayward and Calaveras Faults.* Proceedsing of the Third Conference on Earthquake Hazards in the Eastern San Francisco Bay Area - Science, Hazard, Engineering and Risk, California Geological Survey Special Publication.

Mori, J. & Abercrombie, R. E., 1997. Depth dependence of earthquake frequency-magnitude distributions in California: Implication for rupture initation. *Journal of Geophysical Research,* 102(B7), pp. 15081-15090.

Najdahmadi, B., Bohnoff, M. & Ben-Zion, Y., 2016. Bimaterial interfaces at the Karadere segment of the North Anatolian Fault, northwestern Turkey. *AGU Publications,* Volume 121, pp. 931-950.

Olsen, K. B. et al., 2006. Strong shaking in Los Angeles expected from southern San Andreas earthquake. *Geophysical Research Letters,* Volume 33, p. L07305.

Ozakin, Y., Ben-Zion, Y., Aktar, M. & Karabulut, H., 2012. Velocity contrast across the 1944 rupture zone of the North Anatolian fault east of Ismetpasa from analysis of teleseismic arrivals. *Geophysical Research Letters,* Volume 39.

Reches, Z. & Lockner, D. A., 2010. Fault weakening and earthquake instability by powder lubrication. *Nature,* Volume 467, pp. 452-455.

Rempe, M. et al., 2013. Damage and seismic velocity structure of pulverized rocks near the Sand Andreas Fault. *Journal of Geophysical Research: Solid Earth,* Volume 118, pp. 2813-2831.

Richter, C. F., 1935. An Instrumental Earthquake Magnitude Scale. *Bulletin of the Seismological Society of America,* 25(1), pp. 1-32.

Rouet-Leduc, B., Hulbert, C. & Johnson, P. A., 2019. Continuous chatter of the Cascadia subduction zone revealed by machine learning. *Nature Geoscience,* Volume 12, pp. 75-79.

Rubin, A. M. & Ampuero, J.-P., 2007. Aftershock asymmetry on a bimaterial interface. *Journal of Geophysical Research,* Volume 112, p. B05307.

Scholz, C. H., 1968. The frequency-magnitude relation of microfracturing in rock and its relation to earthquakes. *Bulletin of the Seismological Society of America,* 58(1), pp. 399-415.

Schorlemmer, D., Wiemer, S. & Wyss, M., 2005. Variations in earthquake-size distribution across different stress regimes. *Nature,* Volume 437, p. 539.

Shapiro, S. A. & Kneib, G., 1993. Seismic attenuation by scattering: theory and numerical results. *Geophyscial Journal International,* Volume 114, pp. 373-391.

Shi, Z. & Ben-Zion, Y., 2009. Seismic radiation form tensile and shear point dislocations between similar and dissimilar solids. *Geophysical Journal International,* Volume 179, pp. 444-458.

Shlomai, H. & Fineberg, J., 2016. The structure of slip-pulses and supershear ruptures driving slip in bimaterial friction. *Nature Communications.*

The MathWorks, Inc., 2019. *Signal Processing Toolbox Getting Started Guide.* [Online] Available at: https://www.mathworks.com/help/pdf_doc/signal/signal_gs.pdf [Accessed 6 May 2019].

Thompson , G. & Reyes, C., 2019. *GISMO a seismic data analysis toolbox for MATLAB.* [Online] Available at: https://geoscience-community-codes.github.io/GISMO/ [Accessed 6 May 2019].

Thurber, C. et al., 2006. Three-Dimensional Compressional Wavespeed Model, Earthquake Relocations, Focal Mechanisms for the Parkfield, California, Region. *Bulletin of the Seismological Society of America,* 96(4B), pp. S38-S49.

Townend, J. et al., 2013. Late-interseismic state of a continental plate-bounding fault: Petrophysical results form DFDP-1 wireline logging and core analysis, Alpine Fault, New Zealand. *Geochemistry, Geophysics, Geosystems,* 14(9), pp. 3801-3820.

Weertman, J., 1980. Unstable slippage across a fault that separates elastic media of different elastic constants. *Journal of Geophysical Research,* 85(B3), pp. 1455-1461.

Xia, K., Rosakis, A. J., Kanamori, H. & Rice, J. R., 2005. Laboratory Earthquakes Along Inhomogeneous Faults: Directionality and Supershear. *Science,* 308(5722), pp. 681-684.

Yang, W. et al., 2015. Velocity contrast along the rupture zone of the 2010 Mw6.9 Yushu, China, earthquake form fault zone head waves. *Earth and Planetary Science Letters,* Volume 416, pp. 91-97.

Zaliapin, I. & Ben-Zion, Y., 2011. Asymmetric distribution of aftershocks on large faults in California. *Geophysical Journal International,* Volume 185, pp. 1288-1304.

Appendix A Extended Methodology

There are a total of 9 experimental combinations in this research (Figure A.1). When showing data involving all 9 experimental combinations, I use a 3x3 matrix. The columns represent the top block, while the rows represent the bottom block. An important note, as the 4 accelerometers are located on the top block.

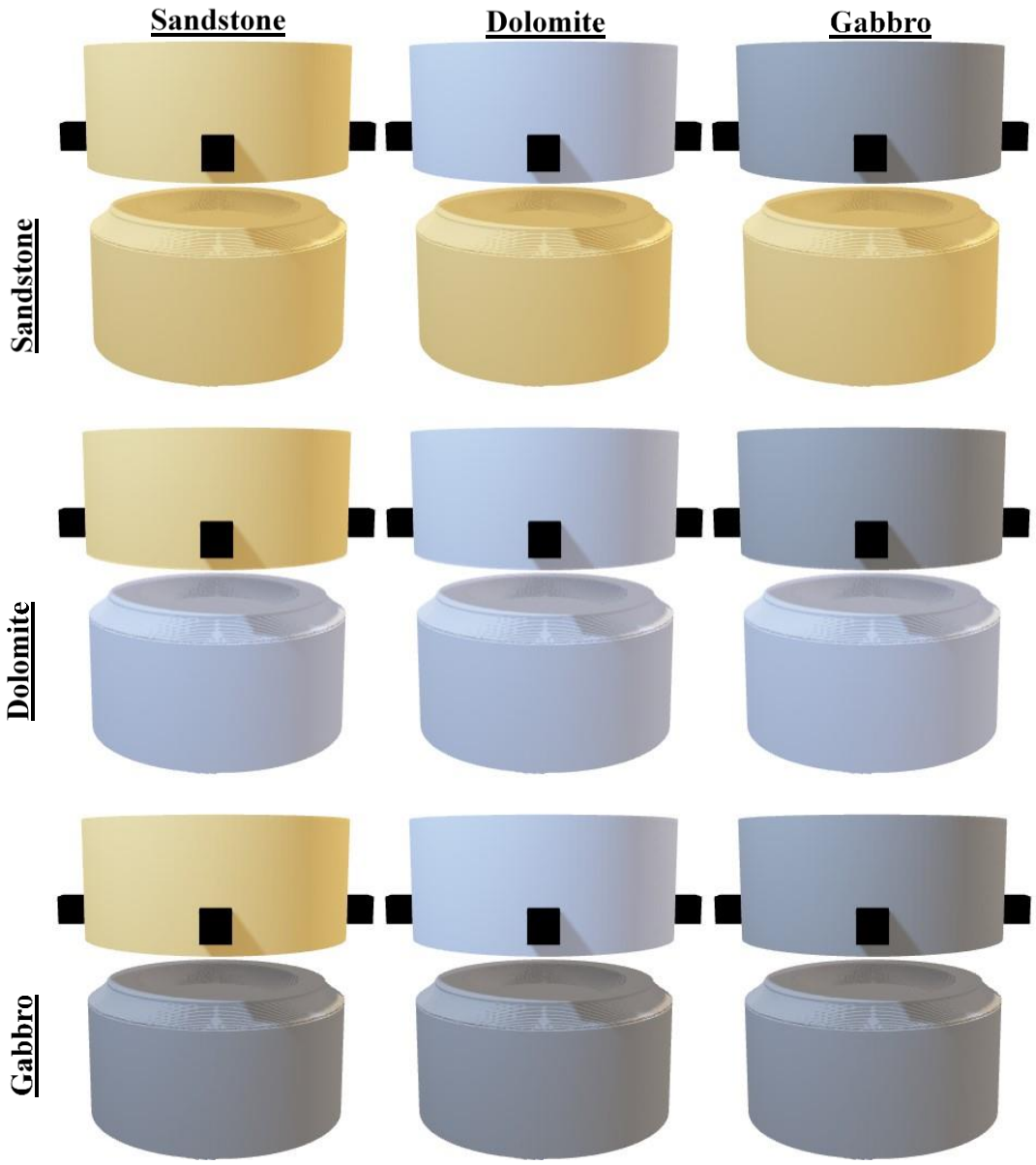

Figure A.1 3D Models for all 9 experimental combinations.

Programs

I developed and used multiple programs to assist with acoustic emission analysis. The programs include: Spectral_analysis_v3, GRLAW, and Wavelet_spectrogram_v3.

On average, each acoustic emission recording includes 16 channels (4 accelerometers with x, y, z, and encoder) of 14 seconds recorded at 1 MHz; that is a total of at least 224,000,000 data samples in a file. To assist in the interpretation and figure development of large acoustic emission datasets, I developed a program and *matlab* scripts to visualize and process the data in both time- and frequency-domains (Figure A.2).

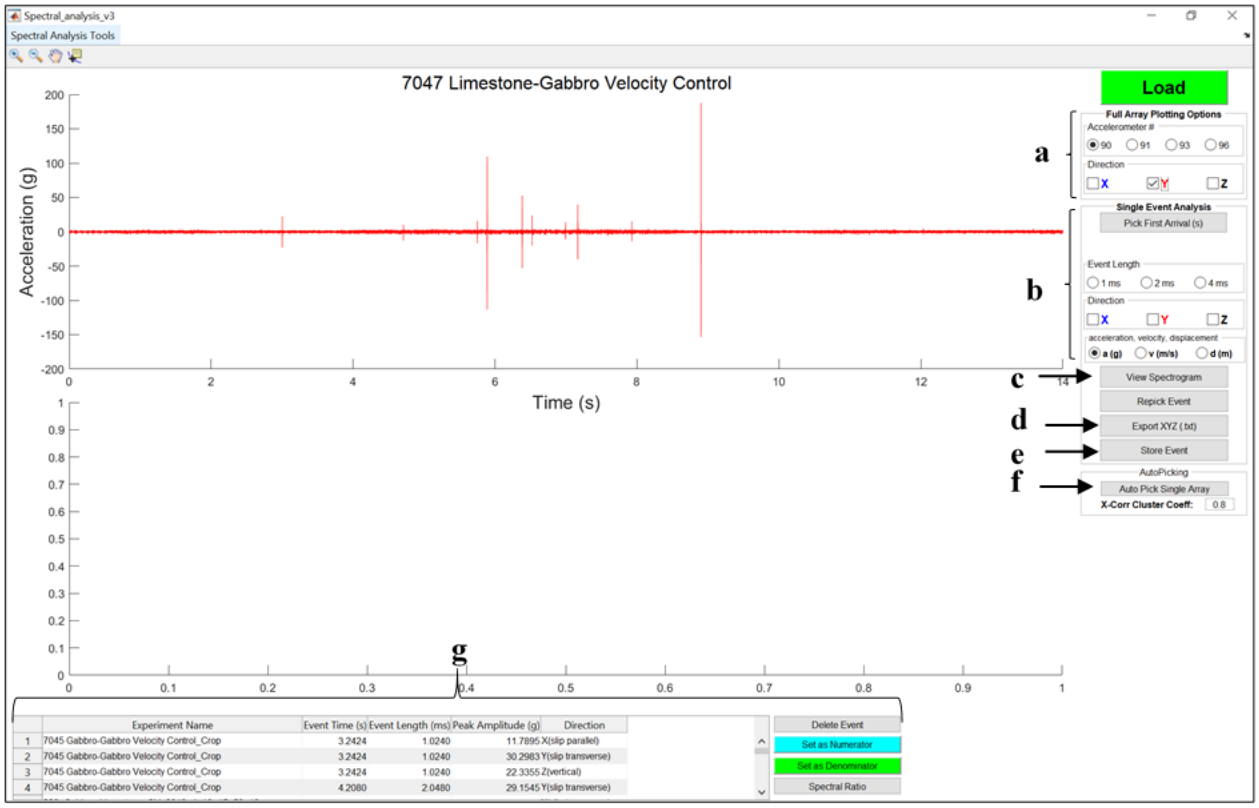

Figure A.2 An image of the Spectral Analysis v3 program I developed in *Matlab* to study acoustic emissions.

Spectral Analysis version 3 allows for: visualizing raw acoustic emissions for all three spatial directions and all four accelerometers (Figure A.2a), manual picking of single events with capabilities to visualize that event in the x, y, and z directions and in acceleration (default),

velocity, and displacement; and the frequency domain (Figure A.2b), visualizing the spectrogram of a single event (button in Figure A.2c; popup spectrogram shown in Figure A.3), exporting the event as a text file (Figure A.2d), storing the event for later processing (Figure A.2e), a single acoustic emission array to be auto-picked (Figure A.2f) by a program developed by GISMO (Thompson & Reyes, 2019) and the comparison of events from different experiments or recording via spectral ratio (Figure A.2g).

I used the relationship between occurrence and peak amplitude of events to show the Gutenberg-Richter relationship of the acoustic events in the present experiments. The following *matlab* script shows how the relationship was plotted. Note that the input is an array of peak amplitudes, the outputs are N (the occurrence) and Amp ($\log_{10}$ peak amplitude), and the number of bins is determined by the square root of the total number of events.

```
function [N,Amp] = GRLAW(PeakAmpEvents)
%GRLAW takes the peak amplitude of the acoustic events to create a
%   occurrence vs peak amplitude plot similar to the Gutenberg-Richter Law
%   (GRLAW).
%
%   Input:
%       PeakAmpEvents: a list of peak amplitude of the acoustic events.
%           (format is double)
%   Output:
%       Amp: is analogous to magnitude M in GRLAW.
%       N: from the GRLAW, N is the number of events greater than or equal
%           to Amp.

    % Takes the log(base 10) of the Peak Amplitude.
    LOGPeakAmp = log10(PeakAmpEvents);

    %----------------------------Optional-----------------------------------
    % Does not count events that are less than -2.5.
    LOGPeakAmp(LOGPeakAmp < -2.5) = nan;
    %----------------------------Optional-----------------------------------

    % Determining the number of events in each bin.
    nbins = round(sqrt(numel(LOGPeakAmp)));
    LOGPeakAmp(imag(LOGPeakAmp)~=0) = nan; % ignores non-real #'s after log
    [count,binedges] = histcounts(LOGPeakAmp,nbins);

    % Determining N(y-axis) and Amp(x-axis).
    for i = 1:nbins
        N(i) = sum(count(i:end));
    end
    N = log10(N);
end
```

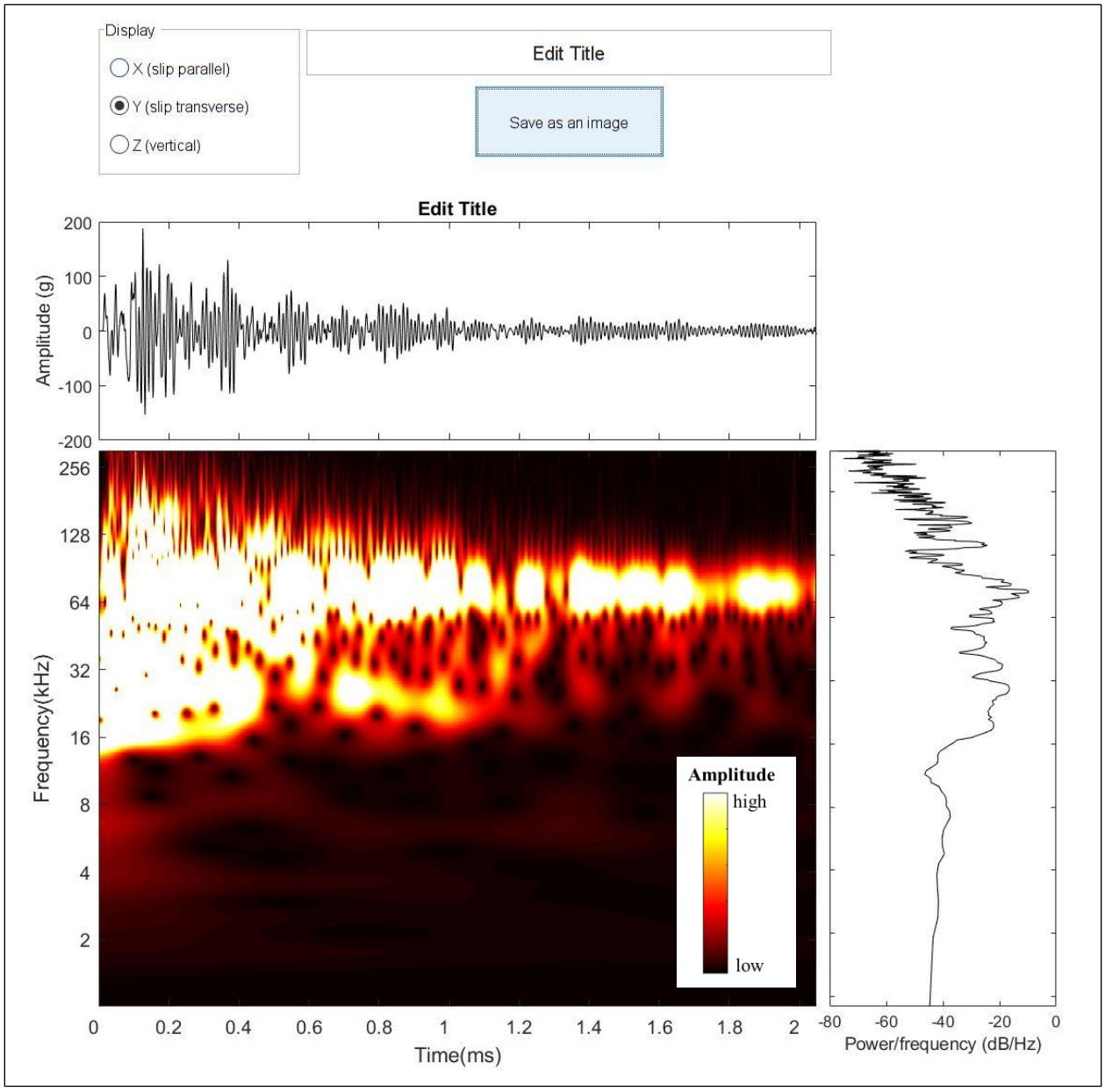

Figure A.3 Image of Wavelet Spectrogram v3 program. Takes a single event from Spectral Analysis v3 and creates an accelerogram, spectrogram, and power spectrum of that event. The code is below.

The Wavelet Spectrogram version 3 program (Figure A.3) is a popup of and must be called from Spectral Analysis v3. It takes a short window of acoustic emission data and provides the accelerogram, spectrogram, and power/dB spectrum. The function that plots these three graphs are shown below. Note that the colormap used in the spectrogram is called ‘hot’; the color map is centered about the median, where the min and max limits are ± the standard deviation.

```
function Plot_Spectrogram(hObject,eventdata,handles)
    % Get data from Spectral_Analysis_v3
    Event_Array = get(handles.Display,'UserData');

    % Spectrogram
    axes(handles.axes1)
    Fs = 1000000; % Sampling Rate
    % calculated the coninuos wavelet transform
    [wt,f] = cwt(Event_Array,'morse',Fs,'ExtendedSignal',true,...
        'VoicesPerOctive',48,'TimeBandwidth',30);
    % calculates statistics for colorbar of spectrogram
    Median = median(reshape(abs(wt),[],1));
    STD = std(reshape(abs(wt),[],1));
    upper_lim = Median+STD;
    % plots spectrogram
    imagesc([],f,abs(wt));
    % set the tick labels for frequency on the y-axis
    if size(get(gca,'YTickLabel'),1) == 8
        set(gca,'YTickLabel',{'2','4','8','16','32','64','128','256'});
    elseif size(get(gca,'YTickLabel'),1) == 9
        set(gca,'YTickLabel',{'1','2','4','8','16','32','64','128','256'});
    end
    % adjusts the axis
    set(gca,'YDir','normal');
    X_Lim = get(gca,'XLim');
    X_Lim(1,1) = 0;
    set(gca,'XLim',X_Lim);
    set(gca,'XTickLabel',get(gca,'XTick')/1000);
    % Axes labels
    set(get(gca,'YLabel'),'String','Frequency(kHz)');
    set(get(gca,'XLabel'),'String','Time(ms)');
    % applies the colormap called 'hot'
    caxis([0 upper_lim]);
    colormap hot
    colorbar off

    % Accelerogram
    % plots accelerogram
    axes(handles.axes2)
    plot(Event_Array,'k');
    Length = length(Event_Array(:,1));
    xlim([0 Length]);
    set(gca,'Xticklabel',[])
    ylabel 'Amplitude (g)'
    Edit_Title_Callback(hObject, eventdata, handles)

    % Power Spectrum
    axes(handles.axes3)
    % calculated the multitaper power spectral density estimate
    [p,fq] = pmtm(Event_Array,4,length(Event_Array),Fs);
    % The following allows for the plot to be plotted on its side
    plot(4*log(p),log2(fq));
    set(gca,'Ydir','normal')
    set(gca,'Yticklabel',[])
    set(gca,'YLabel',[]);
    set(get(gca,'Children'),'Color',[0 0 0])
    set(gca,'Title',[]);
    y = log2(f);
    ylim([y((length(y)),1) y(1,1)])
    set(get(gca,'XLabel'),'String','Power/frequency (dB/Hz)');
```

Appendix B Supplementary Material from Chapter 3

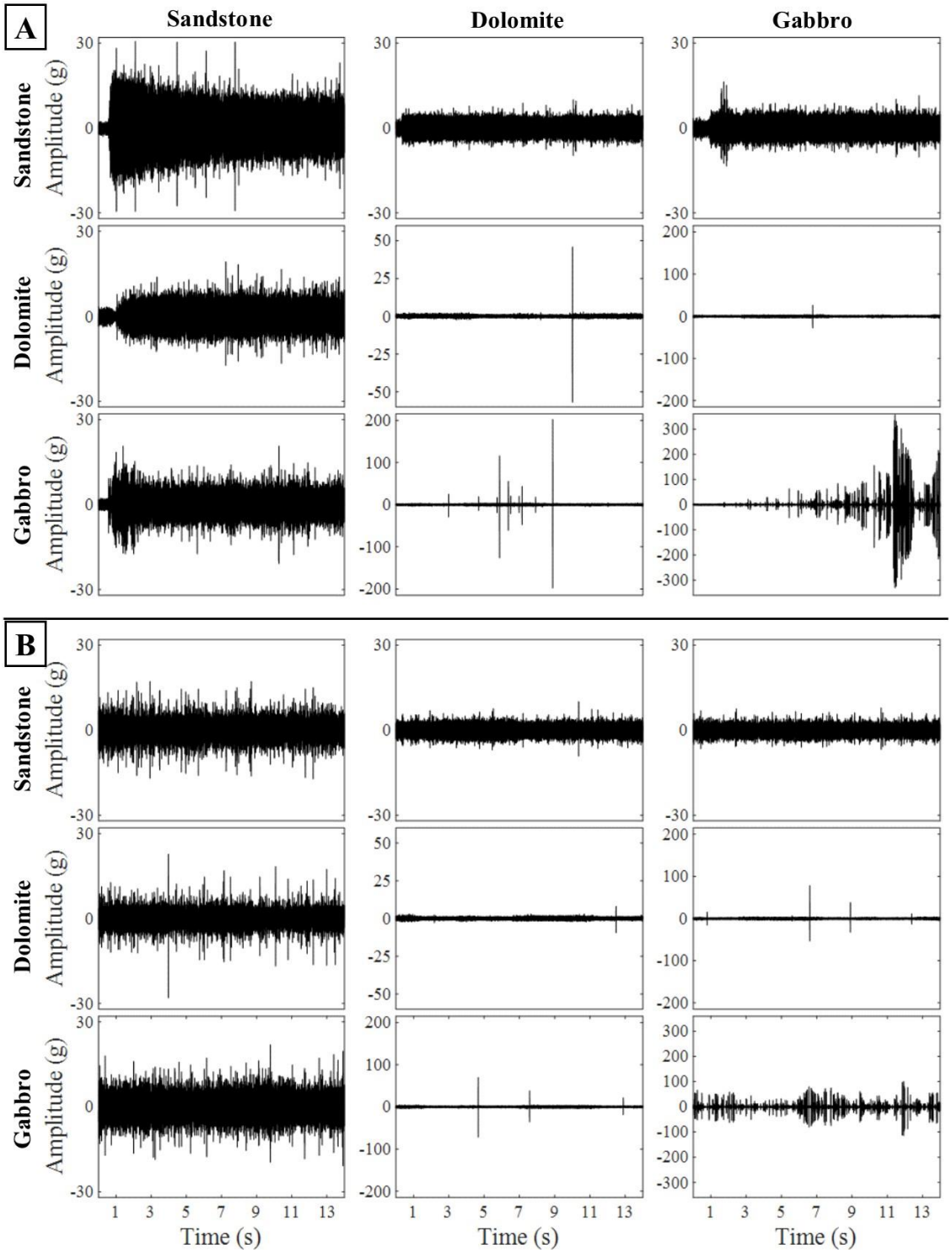

Figure B.1 Accelerograms of raw acoustic emissions in the y transverse direction from experiments sheared at 1 mm/s along (A) fresh fault surfaces and (B) worn fault surfaces. Each accelerogram represents a rock-block combination where columns represent the side with accelerometers and rows represent the opposing side.

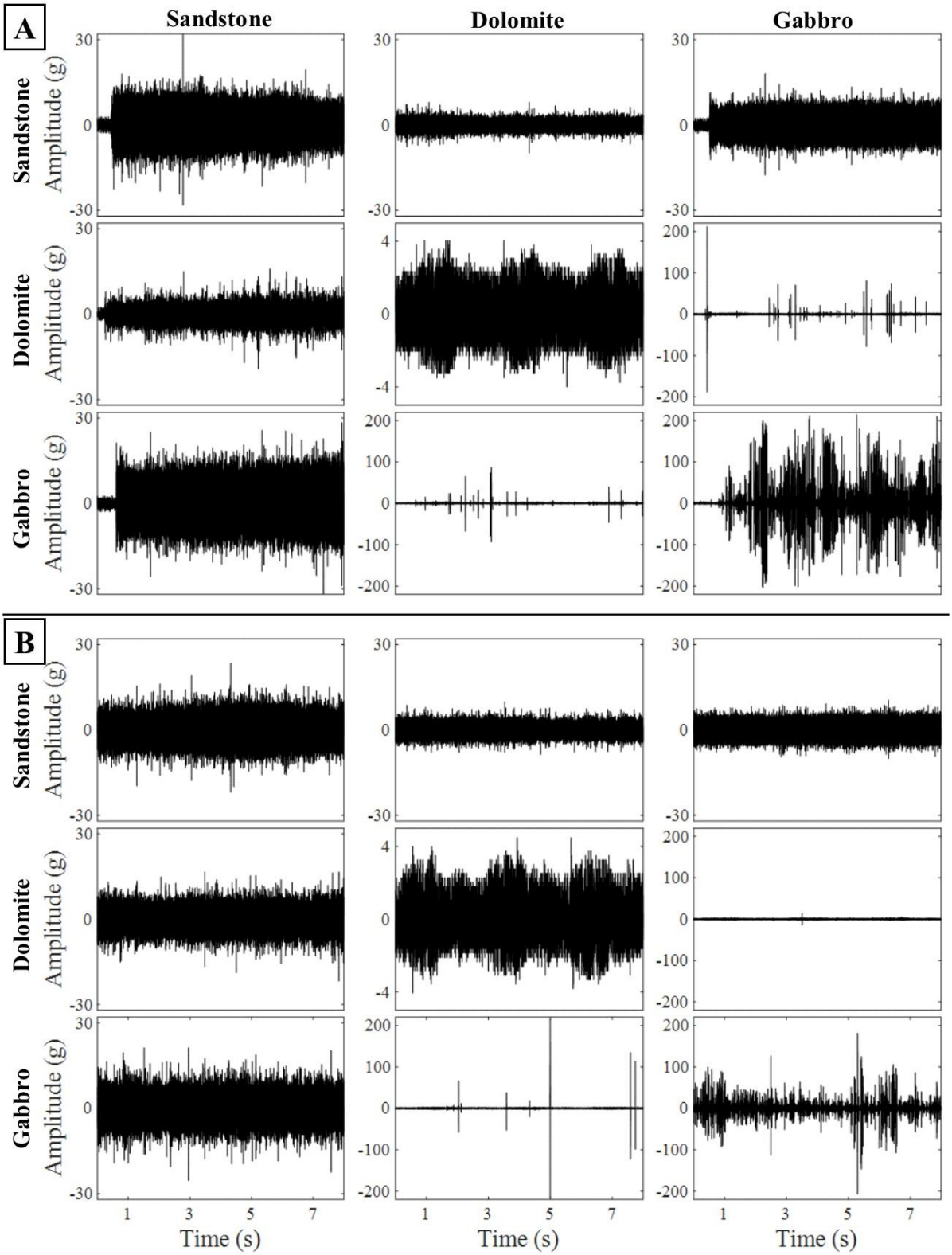

Figure B.2 Accelerograms of raw acoustic emissions in the y transverse direction from experiments sheared at 1 cm/s along (A) fresh fault surfaces and (B) worn fault surfaces. Each accelerogram represents a rock-block combination where columns represent the side with accelerometers and rows represent the opposing side.

Acoustic emissions along all possible experimental combinations show varying behaviors (Figures B.1 and B.2). Experiments that contain sandstone have acoustic emissions that look like seismic chatter, while each individual spike in gabbro and/or dolomite experiments are distinct acoustic events resembling natural earthquakes.

Furthermore, Figure B.3 shows an accelerogram, spectrogram, and power spectrum of noise levels the accelerometers record before the motors starts. The noise levels are significantly smaller than the acoustic emissions in Figures B.1 and B.2 showing that the recording are signals rather than noise.

Prior to the auto-picking program, events in gabbro and/or dolomite experiments were manually picked. To confirm that the auto-picking was accurate, I compared the manual and auto picking using a Gutenberg-Richter relationship plot to show that they are similar (Figure B.4).

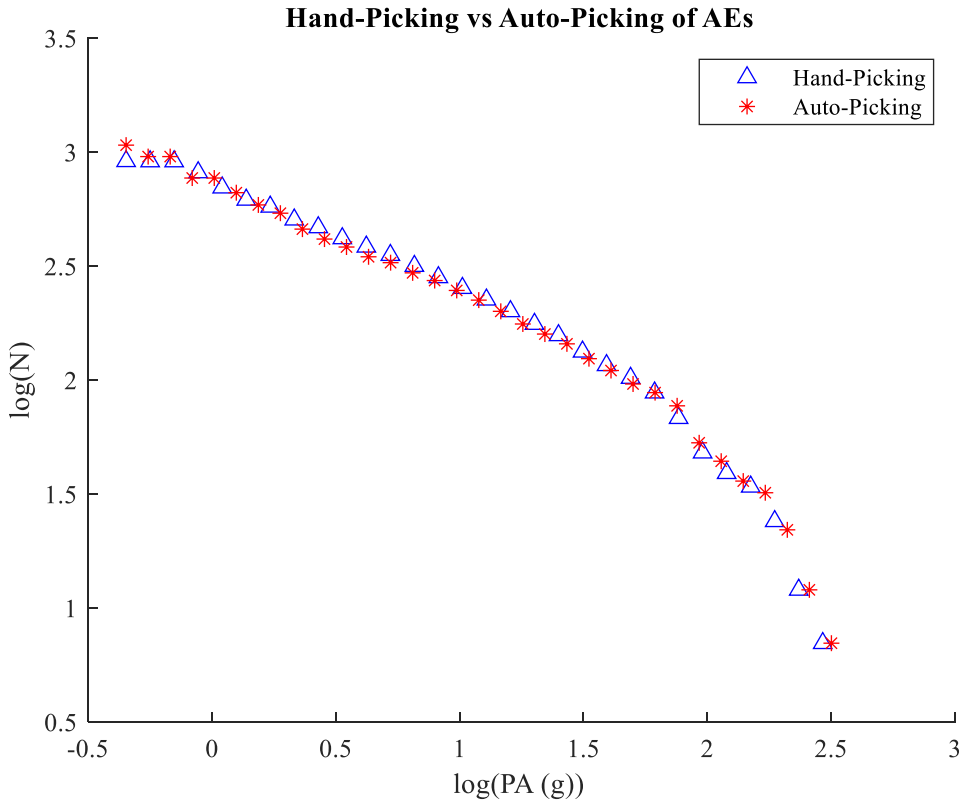

Figure B.3 Occurrence and peak amplitude relationship comparing hand-picked events vs auto-picked events. This plot shows that auto-picking is accurate.

Figures B.5, B.6, and B.7 show the occurrence vs peak amplitude plots comparing x, y, and z directions for 1 mm/s along a worn surface, 1 cm/s along a fresh surface, and 1cm/s along a worn surface, respectively. I compare the x, y, and z directions for every accelerometer along the possible experimental pairs of gabbro and dolomite. The three direction show similar behaviors with each other; I then take the geometric mean of the single events in the three directions (Figures 3.4, 3.5, 3.6, and 3.7).

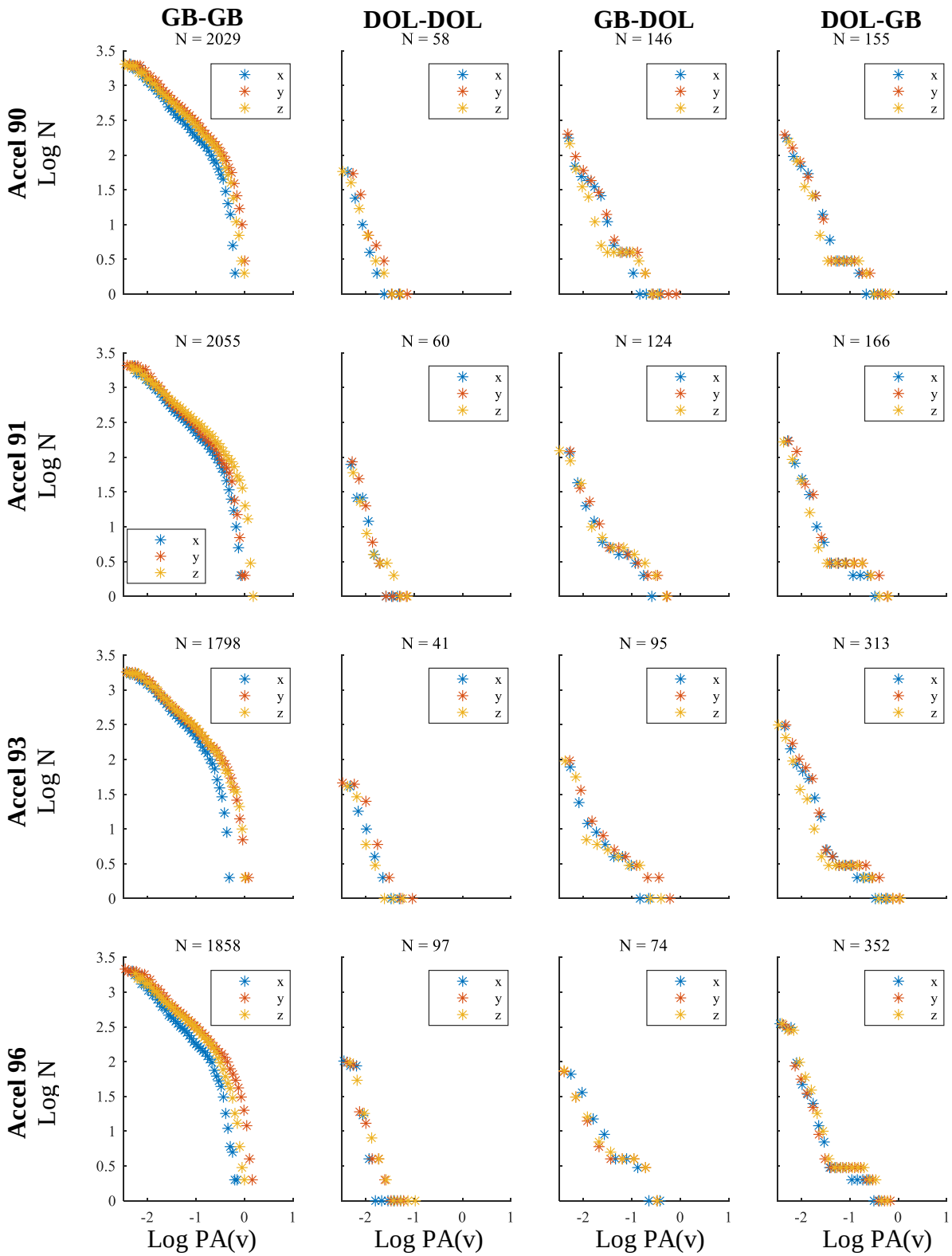

Figure B.4 Occurrence (N) vs peak amplitude (PA) plots showing the x, y, z spatial directions for the 4 accelerometers and the 4 experimental combinations sheared along worn fault surfaces at 1 mm/s.

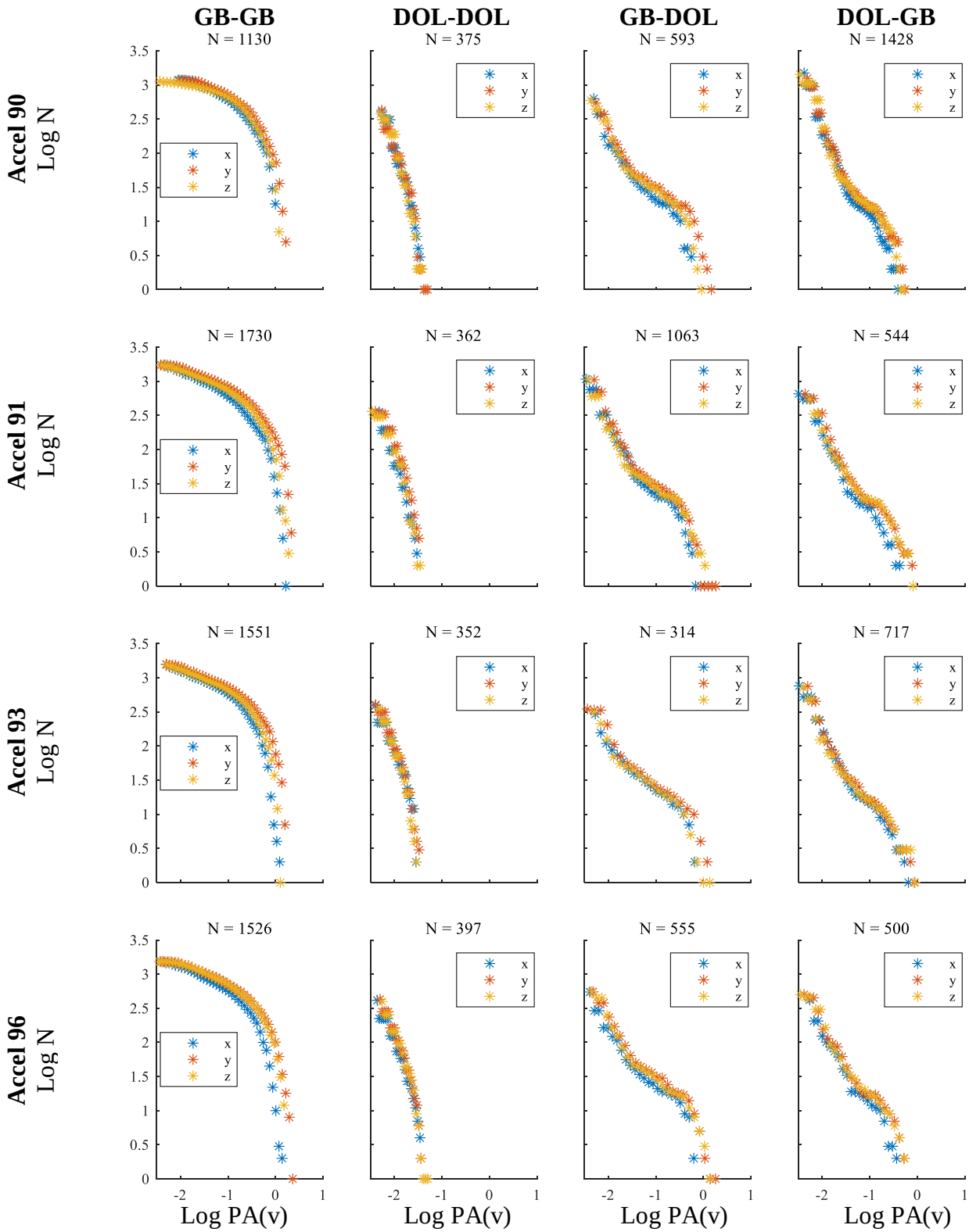

Figure B.5 Occurrence (N) vs peak amplitude (PA) plots showing the x, y, z spatial directions for the 4 accelerometers and the 4 experimental combinations sheared along fresh fault surfaces at 1 cm/s.

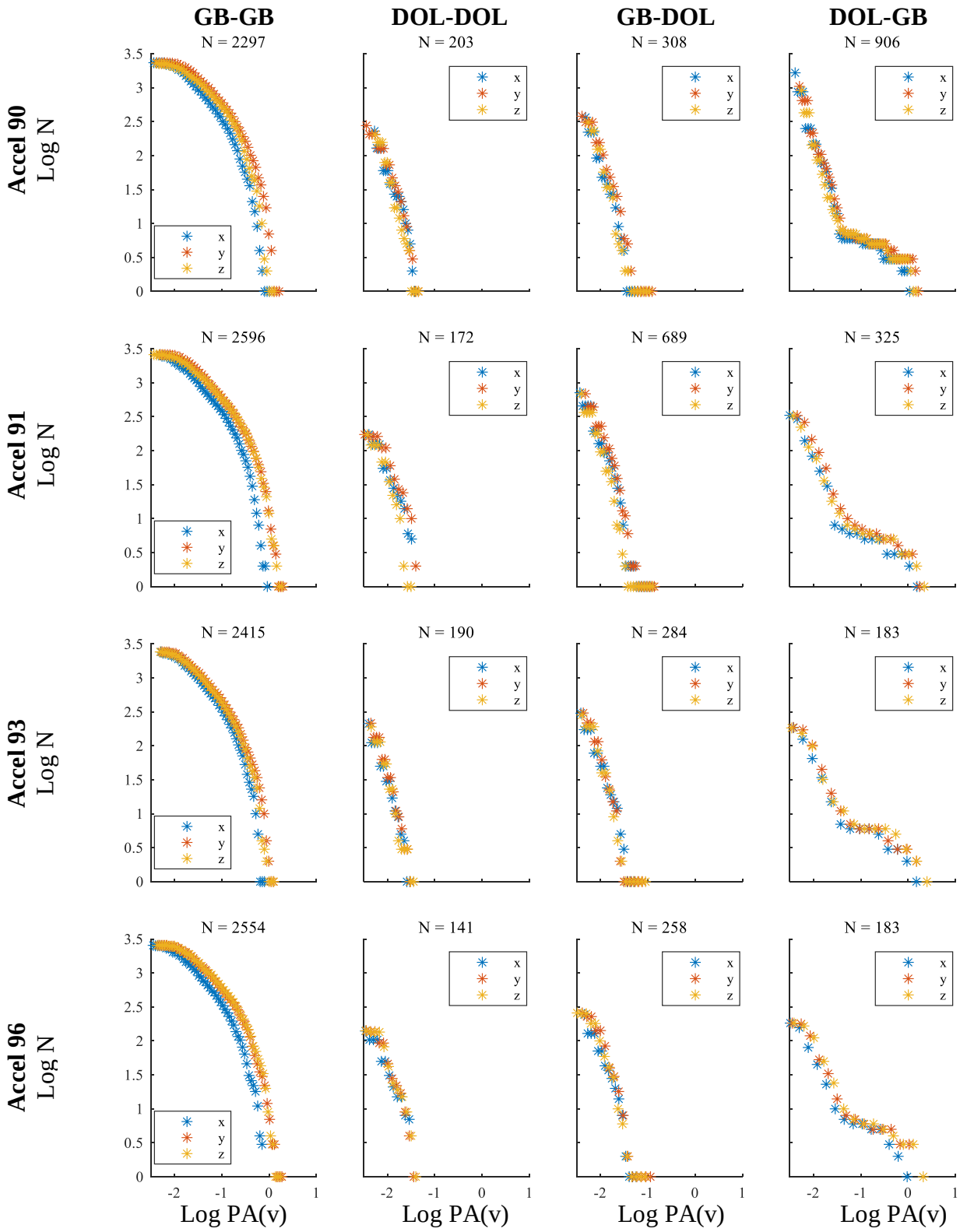

Figure B.6 Occurrence (N) vs peak amplitude (PA) plots showing the x, y, z spatial directions for the 4 accelerometers and the 4 experimental combinations sheared along worn fault surfaces at 1 cm/s.

The figure below (Figure B.8) shows occurrence (N) vs peak amplitude (PA) plots of the complete combination from the four recordings of 1 mm/s and 1 cm/s along both fresh and worn surfaces. The plots show the distinct behavioral difference between the experimental pairs. GB-GB has the most events with the largest events, while DOL-DOL has the least number of events and only has small events. GB-DOL and DOL-GB have an intermediate number of events with a bimodal distribution on the N vs PA relationship.

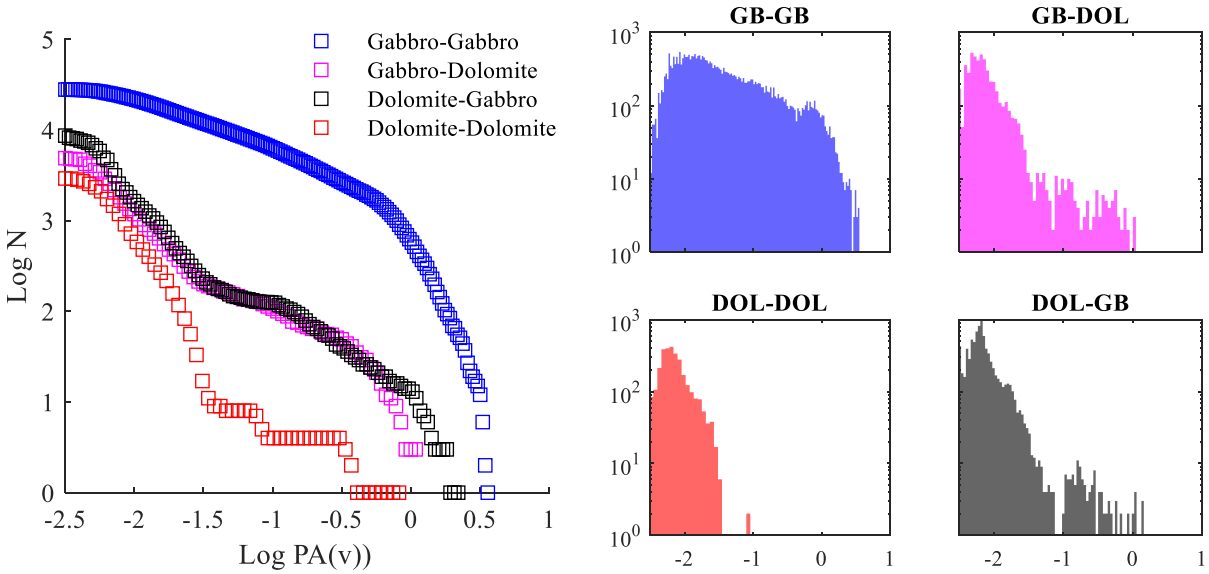

Figure B.7 Occurrence vs peak amplitude relationship by combining datasets of fresh, worn, 1 mm/s, and 1 cm/s for each experimental combination. Shown is their corresponding histogram.

Appendix C Supplementary Material from Chapter 4

I make a comparison of two similar size events; one event was created from GB-GB (Figure C.1) and the other from GB-DOL (Figure C.2). Since both events have the same ray path (i.e. gabbro), the differences in behavior must be due to source effects.

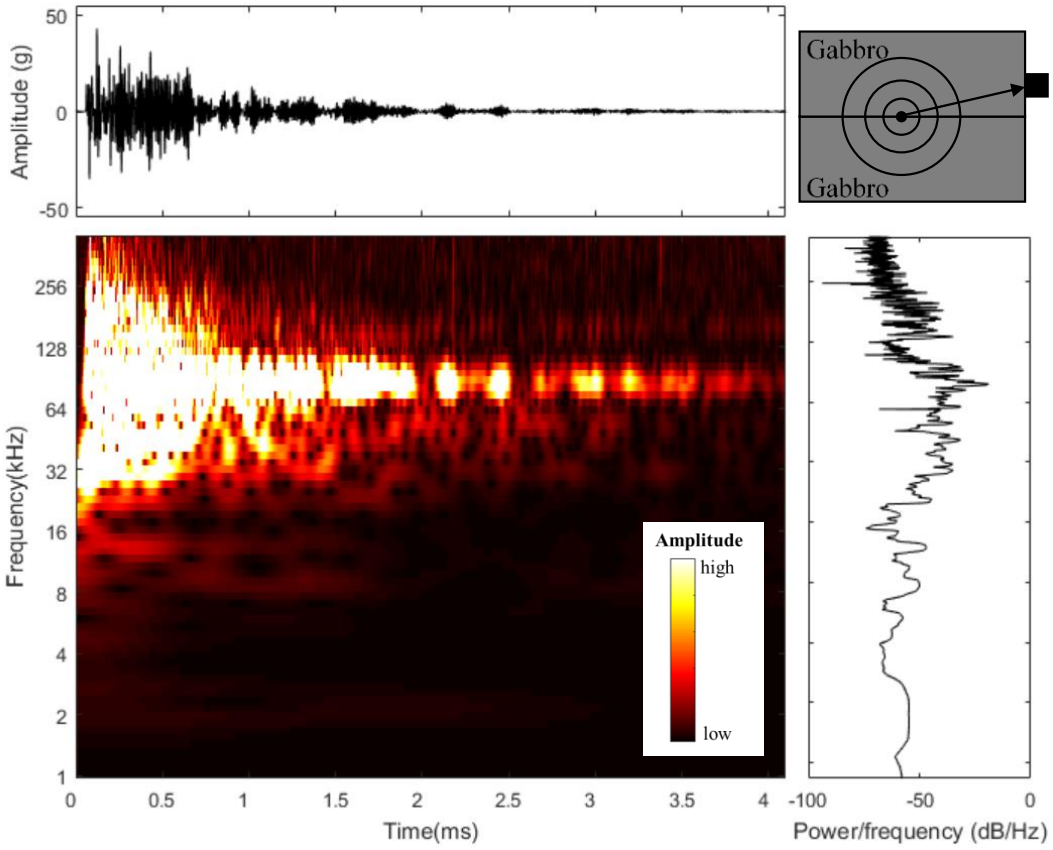

Figure C.1 Accelerogram, spectrogram, and power spectrum of a single event in a gabbro-gabbro experiment. The acoustic event is 4ms in duration with a peak amplitude of 46g. The frequency band at ~80 kHz is due to machine response and is ignored for comparisons. This event is compared with the event in Figure C.2.

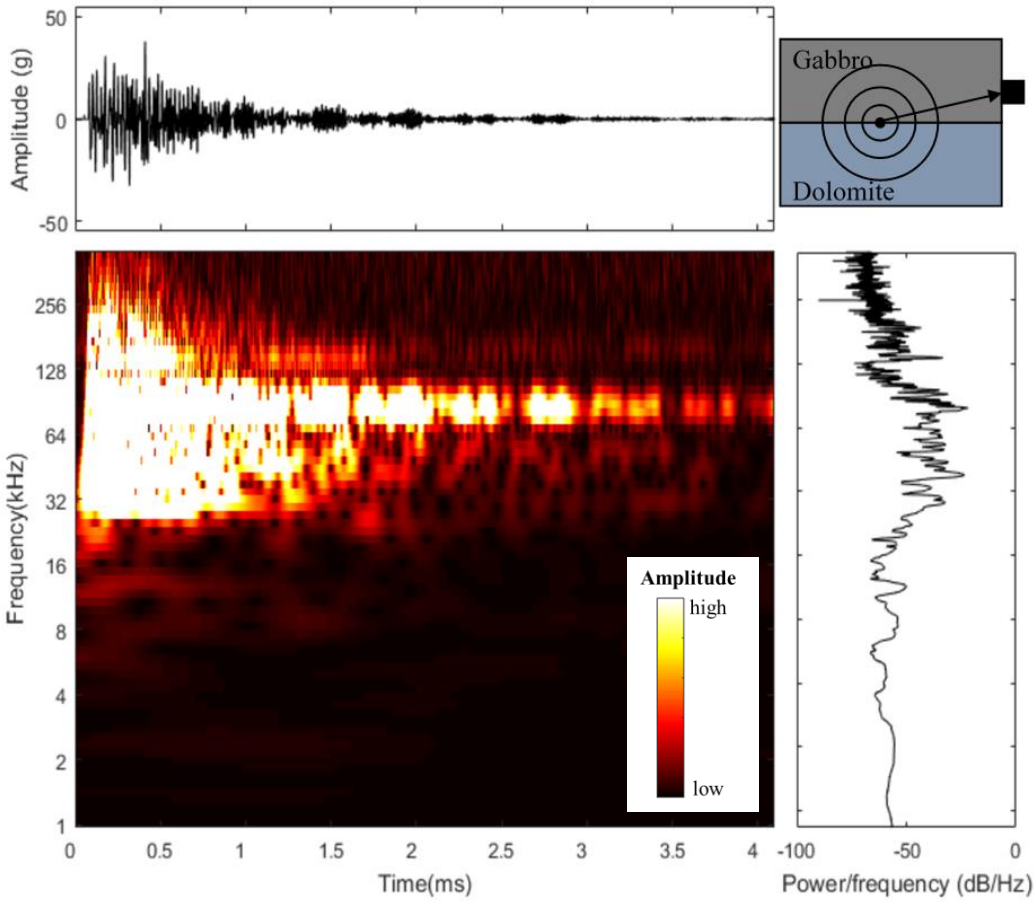

Figure C.2 Accelerogram, spectrogram, and power spectrum of a single event in a gabbro-dolomite experiment. The acoustic event is 4ms in duration with a peak amplitude of 44g. The frequency band at ~80 kHz is due to machine response and is ignored for comparisons. This event is compared with the event in Figure C.1.

Appendix D Bi-material Experiments List

Table D-1 List of bi-material experiments

Exp #	Top Block	Bottom Block	σ_N (MPa)	AE?	Shear Velocity
7000	Gabbro	Sandstone	1.5	Yes	1 cm/sec
7001	Gabbro	Sandstone	1.5	Yes	1 cm/sec
7004	Gabbro	Gabbro	1.4	Yes	1 cm/sec
7005	Gabbro	Gabbro	1.4	Yes	1 cm/sec
7018	Sandstone	Sandstone	1.5	Yes	1 cm/sec
7019	Dolomite	Dolomite	1.4	Yes	1 cm/sec
7020	Dolomite	Dolomite	0.6	Yes	1 cm/sec
7021	Sandstone	Dolomite	0.6	Yes	1 cm/sec
7022	Gabbro	Dolomite	0.6	Yes	1 cm/sec
7023	Gabbro	Gabbro	0.6	Yes	1 cm/sec
7024	Gabbro	Sandstone	0.6	Yes	1 cm/sec
7025	Sandstone	Sandstone	0.6	Yes	1 cm/sec
7026	Dolomite	Dolomite	0.6	Yes	1 cm/sec
7028	Sandstone	Gabbro	0.7	Yes	1 cm/sec
7029	Sandstone	Gabbro	0.7	Yes	1 cm/sec
7030	Dolomite	Gabbro	0.6	Yes	1 cm/sec
7031	Dolomite	Gabbro	0.6	Yes	1 cm/sec
7032	Sandstone	Gabbro	0.7	Yes	1 cm/sec
7033	Dolomite	Gabbro	0.6	Yes	1 cm/sec
7042	Gabbro	Sandstone	0.7	Yes	1 mm/sec
7043	Dolomite	Sandstone	0.7	Yes	1 mm/sec
7044	Sandstone	Dolomite	0.7	Yes	1 mm/sec
7045	Gabbro	Gabbro	0.7	Yes	1 mm/sec
7046	Gabbro	Dolomite	0.7	Yes	1 mm/sec
7047	Dolomite	Gabbro	0.7	Yes	1 mm/sec
7048	Sandstone	Sandstone	0.8	Yes	1 mm/sec
7049	Sandstone	Gabbro	0.8	Yes	1 mm/sec
7050	Dolomite	Dolomite	0.7	Yes	1 mm/sec
7170	Sandstone	Sandstone	2.0	No	10 μm/sec
7171	Sandstone	Sandstone	2.0	No	10 μm/sec
7172	Sandstone	Sandstone	2.0	No	1,10,100 μm/sec
7173	Sandstone	Sandstone	2.0	No	1,10,100 μm/sec
7174	Sandstone	Sandstone	2.0	No	1,10,100 μm/sec
7175	Dolomite	Sandstone	2.1	No	10 μm/sec
7176	Dolomite	Sandstone	2.1	No	10 μm/sec
7177	Dolomite	Sandstone	2.1	No	1,10,100 μm/sec
7178	Dolomite	Sandstone	2.1	No	1,10,100 μm/sec
7179	Sandstone	Dolomite	2.1	No	10 μm/sec
7180	Sandstone	Dolomite	2.2	No	10 μm/sec
7181	Sandstone	Dolomite	2.2	No	1,10,100 μm/sec
7182	Sandstone	Dolomite	2.2	No	1,10,100 μm/sec
7183	Dolomite	Dolomite	2.1	No	10 μm/sec
7184	Dolomite	Dolomite	2.2	No	10 μm/sec
7185	Dolomite	Dolomite	2.2	No	1,10,100 μm/sec
7186	Dolomite	Dolomite	2.2	No	1,10,100 μm/sec
7187	Dolomite	Dolomite	2.2	No	1,10,100 μm/sec

7188	Gabbro	Dolomite	2.1	No	10 µm/sec
7189	Gabbro	Dolomite	2.1	No	10 µm/sec
7190	Gabbro	Dolomite	2.1	No	1,10,100 µm/sec
7191	Gabbro	Dolomite	2.1	No	1,10,100 µm/sec
7193	Dolomite	Gabbro	2.0	No	10 µm/sec
7194	Dolomite	Gabbro	2.0	No	1,10,100 µm/sec
7195	Dolomite	Gabbro	2.0	No	1,10,100 µm/sec
7196	Dolomite	Gabbro	2.0	No	1,10,100 µm/sec
7197	Gabbro	Gabbro	2.0	No	10 µm/sec
7198	Gabbro	Gabbro	2.1	No	10 µm/sec
7199	Gabbro	Gabbro	2.1	No	1,10,100 µm/sec
7200	Gabbro	Gabbro	2.1	No	1,10,100 µm/sec
7201	Gabbro	Gabbro	2.1	No	1,10,100 µm/sec
7202	Gabbro	Gabbro	2.1	No	1,10,100 µm/sec
7203	Gabbro	Sandstone	2.0	No	10 µm/sec
7204	Gabbro	Sandstone	2.0	No	10 µm/sec
7205	Gabbro	Sandstone	2.0	No	1,10,100 µm/sec
7206	Gabbro	Sandstone	2.0	No	1,10,100 µm/sec
7207	Gabbro	Gabbro	2.0	No	1,10,100 µm/sec
7208	Sandstone	Gabbro	2.0	No	10 µm/sec
7209	Sandstone	Gabbro	2.0	No	10 µm/sec
7210	Sandstone	Gabbro	2.0	No	1,10,100 µm/sec
7211	Sandstone	Gabbro	2.0	No	1,10,100 µm/sec
7212	Sandstone	Gabbro	2.0	No	1,10,100 µm/sec
7213	Gabbro	Gabbro	6.5	No	10 µm/sec
7214	Gabbro	Gabbro	6.3	No	10 µm/sec
7215	Gabbro	Gabbro	6.2	No	10 µm/sec
7216	Gabbro	Gabbro	6.2	No	50 µm/sec
7217	Gabbro	Gabbro	6.2	No	200 µm/sec
7218	Gabbro	Gabbro	6.2	No	200 µm/sec
7219	Gabbro	Gabbro	6.3	No	200 µm/sec
7220	Gabbro	Gabbro	6.0	Yes	200 µm/sec
7221	Gabbro	Gabbro	5.9	Yes	200 µm/sec
7222	Gabbro	Gabbro	5.8	Yes	335 µm/sec
7223	Gabbro	Sandstone	6.3	No	200 µm/sec
7224	Gabbro	Sandstone	6.2	No	10 µm/sec
7225	Gabbro	Sandstone	6.1	No	200 µm/sec
7226	Gabbro	Sandstone	6.1	No	200 µm/sec
7227	Gabbro	Dolomite	6.2	No	10 µm/sec
7228	Gabbro	Dolomite	6.2	Yes	200 µm/sec
7229	Gabbro	Dolomite	6.2	Yes	200 µm/sec
7230	Gabbro	Dolomite	10.5	No	10 µm/sec
7231	Gabbro	Dolomite	10.5	No	10 µm/sec
7232	Gabbro	Dolomite	10.5	Yes	100 µm/sec
7233	Gabbro	Dolomite	10.5	No	100 µm/sec
7234	Gabbro	Dolomite	10.5	Yes	300 µm/sec
7235	Gabbro	Dolomite	10.5	Yes	300 µm/sec
7236	Gabbro	Sandstone	10.3	No	10 µm/sec
7291	Gabbro	Gabbro	9.9	No	10 µm/sec
7292	Gabbro	Gabbro	9.8	Yes	100 µm/sec
7293	Gabbro	Gabbro	9.8	Yes	100 µm/sec
7294	Gabbro	Gabbro	9.8	Yes	200 µm/sec

7295	Gabbro	Gabbro	9.8	Yes	200 µm/sec
7296	Gabbro	Gabbro	9.8	Yes	200 µm/sec
7297	Gabbro	Gabbro	9.8	Yes	300 µm/sec
7298	Gabbro	Gabbro	11.8	No	10 µm/sec
7299	Gabbro	Gabbro	11.8	Yes	10 µm/sec
7300	Gabbro	Gabbro	11.8	No	1 µm/sec
7301	Gabbro	Gabbro	11.8	Yes	0.25 µm/sec
7302	Gabbro	Gabbro	11.8	No	2.5 µm/sec
7303	Gabbro	Gabbro	11.8	No	10 µm/sec
7304	Gabbro	Gabbro	11.8	No	0.25 µm/sec
7305	Gabbro	Gabbro	11.8	No	0.5 µm/sec
7306	Gabbro	Gabbro	11.8	No	1 µm/sec
7307	Gabbro	Gabbro	11.9	No	2 µm/sec
7308	Gabbro	Gabbro	11.9	No	4 µm/sec
7309	Gabbro	Gabbro	11.9	No	8 µm/sec
7310	Gabbro	Gabbro	11.9	No	8 µm/sec
7311	Gabbro	Gabbro	11.9	No	16 µm/sec
7312	Gabbro	Gabbro	11.9	No	12 µm/sec
7313	Gabbro	Gabbro	12.0	No	32 µm/sec
7314	Gabbro	Gabbro	14.2	Yes	10 µm/sec
7315	Gabbro	Gabbro	14.2	Yes	8 µm/sec
7316	Gabbro	Gabbro	14.2	Yes	4 µm/sec
7317	Gabbro	Gabbro	14.2	Yes	2 µm/sec
7318	Gabbro	Gabbro	14.2	Yes	1 µm/sec
7319	Gabbro	Gabbro	14.2	No	0.5 µm/sec
7320	Gabbro	Gabbro	14.2	Yes	0.25 µm/sec
7321	Gabbro	Gabbro	10.2	No	0.25 µm/sec
7322	Dolomite	Gabbro	8.5	No	0.25 µm/sec
7323	Dolomite	Gabbro	8.6	Yes	10 µm/sec
7324	Dolomite	Gabbro	8.6	No	10 µm/sec
7325	Dolomite	Gabbro	8.6	No	0.25 µm/sec
7326	Dolomite	Gabbro	8.6	No	0.5 µm/sec
7327	Dolomite	Gabbro	8.3	No	0.25 µm/sec
7328	Dolomite	Gabbro	8.3	No	1 µm/sec
7329	Dolomite	Gabbro	8.3	No	1 µm/sec
7330	Dolomite	Gabbro	8.3	No	10 µm/sec
7331	Dolomite	Gabbro	8.3	No	10 µm/sec
7332	Dolomite	Gabbro	8.3	Yes	100 µm/sec
7333	Dolomite	Gabbro	8.3	Yes	100 µm/sec
7334	Dolomite	Gabbro	9.9	No	0.25 µm/sec
7335	Dolomite	Gabbro	9.7	No	0.25 µm/sec
7336	Dolomite	Gabbro	9.9	No	1 µm/sec
7337	Dolomite	Gabbro	9.9	Yes	1 µm/sec
7338	Dolomite	Gabbro	9.9	Yes	10 µm/sec
7339	Dolomite	Gabbro	9.9	Yes	10 µm/sec
7340	Dolomite	Gabbro	9.7	Yes	10 µm/sec
7341	Dolomite	Gabbro	9.9	Yes	100 µm/sec
7342	Dolomite	Gabbro	11.7	No	0.25 µm/sec
7343	Dolomite	Gabbro	11.5	Yes	0.25 µm/sec
7344	Dolomite	Gabbro	11.7	Yes	1 µm/sec
7345	Dolomite	Gabbro	11.7	No	1 µm/sec
7346	Dolomite	Gabbro	11.7	Yes	10 µm/sec

7347	Dolomite	Gabbro	11.7	No	10 µm/sec
7348	Dolomite	Gabbro	11.5	Yes	100 µm/sec
7349	Dolomite	Gabbro	11.7	Yes	100 µm/sec
7350	Dolomite	Gabbro	13.6	No	0.25 µm/sec
7351	Dolomite	Gabbro	13.5	Yes	0.25 µm/sec
7352	Dolomite	Gabbro	13.5	No	1 µm/sec
7353	Dolomite	Gabbro	13.5	Yes	1 µm/sec
7354	Dolomite	Gabbro	13.5	Yes	10 µm/sec
7355	Dolomite	Gabbro	13.5	Yes	10 µm/sec
7356	Dolomite	Gabbro	13.5	Yes	100 µm/sec
7357	Dolomite	Gabbro	13.5	Yes	100 µm/sec
7600	Gabbro	Gabbro	9.6	No	1 µm/sec
7601	Gabbro	Gabbro	9.5	No	100 µm/sec
7602	Gabbro	Gabbro	9.6	No	100 µm/sec
7603	Gabbro	Gabbro	9.6	No	100 µm/sec
7604	Gabbro	Gabbro	12.5	No	1 µm/sec
7605	Gabbro	Gabbro	12.5	No	10 µm/sec
7606	Gabbro	Gabbro	12.1	No	10 µm/sec
7607	Gabbro	Gabbro	12.5	Yes	1 µm/sec
7608	Gabbro	Gabbro	12.5	Yes	1 µm/sec
7609	Gabbro	Gabbro	12.5	No	0.25 µm/sec
7610	Gabbro	Gabbro	12.5	No	0.25 µm/sec
7611	Gabbro	Gabbro	15.4	No	1 µm/sec
7612	Gabbro	Gabbro	15.3	Yes	1 µm/sec
7613	Gabbro	Gabbro	15.3	Yes	0.25 µm/sec
7614	Gabbro	Gabbro	15.3	Yes	0.25 µm/sec
7615	Gabbro	Gabbro	14.7	No	0.25 µm/sec
7616	Gabbro	Gabbro	14.7	Yes	0.25 µm/sec
7617	Gabbro	Gabbro	16.2	Yes	0.25 µm/sec
7620	Dolomite	Gabbro	12.7	No	10 µm/sec
7621	Dolomite	Gabbro	12.7	No	10 µm/sec
7622	Dolomite	Gabbro	12.7	No	10 µm/sec
7623	Dolomite	Gabbro	12.7	No	0.25 µm/sec
7624	Dolomite	Gabbro	12.7	No	0.25 µm/sec
7625	Dolomite	Gabbro	12.7	No	5 µm/sec
7626	Dolomite	Gabbro	12.7	No	5 µm/sec
7627	Dolomite	Gabbro	12.7	No	0.25 µm/sec
7630	Gabbro	Gabbro	15.4	No	10 µm/sec
7631	Gabbro	Gabbro	15.3	No	10 µm/sec
7632	Gabbro	Gabbro	15.3	No	10 µm/sec
7633	Gabbro	Gabbro	15.3	No	10 µm/sec
7634	Gabbro	Gabbro	15.3	No	10 µm/sec
7635	Gabbro	Gabbro	15.3	No	1 µm/sec
7636	Gabbro	Gabbro	15.3	No	1 µm/sec
7637	Gabbro	Gabbro	15.3	No	1 µm/sec
7638	Gabbro	Gabbro	15.3	No	0.5 µm/sec
7639	Gabbro	Gabbro	15.3	No	0.5 µm/sec
7640	Gabbro	Gabbro	15.3	No	0.5 µm/sec
7641	Gabbro	Gabbro	15.3	No	0.25 µm/sec
7642	Gabbro	Gabbro	15.3	No	0.25 µm/sec
7643	Gabbro	Gabbro	15.3	No	1 µm/sec
7644	Gabbro	Gabbro	15.3	No	1 µm/sec

7645	Gabbro	Gabbro	15.3	No	2 µm/sec
7646	Gabbro	Gabbro	15.3	No	2 µm/sec
7647	Gabbro	Gabbro	15.4	No	5 µm/sec
7648	Gabbro	Gabbro	15.4	No	5 µm/sec
7649	Gabbro	Gabbro	15.4	No	4 µm/sec
7650	Gabbro	Gabbro	15.5	No	4 µm/sec
7651	Gabbro	Gabbro	15.5	No	4 µm/sec
7652	Gabbro	Gabbro	15.5	No	1 µm/sec
7653	Gabbro	Gabbro	15.6	No	1 µm/sec
7654	Gabbro	Gabbro	15.6	No	0.25 µm/sec
7655	Gabbro	Gabbro	15.6	No	0.25 µm/sec
7656	Gabbro	Gabbro	15.6	No	4.5 µm/sec
7657	Gabbro	Gabbro	15.7	No	4.5 µm/sec
7658	Gabbro	Gabbro	15.7	No	5 µm/sec
7659	Gabbro	Gabbro	15.7	No	5 µm/sec
7660	Gabbro	Gabbro	15.7	No	10 µm/sec
7661	Gabbro	Gabbro	15.7	No	10 µm/sec
7662	Gabbro	Gabbro	15.7	No	8 µm/sec
7663	Gabbro	Gabbro	15.7	No	8 µm/sec
7664	Gabbro	Gabbro	15.7	No	8 µm/sec
7665	Gabbro	Gabbro	15.8	No	8 µm/sec
7666	Gabbro	Gabbro	15.8	No	9 µm/sec
7667	Gabbro	Gabbro	15.8	No	9 µm/sec
7668	Gabbro	Gabbro	15.8	No	9 µm/sec
7669	Gabbro	Gabbro	15.8	No	10 µm/sec
7670	Gabbro	Gabbro	15.8	No	10 µm/sec
7671	Gabbro	Gabbro	15.8	No	10 µm/sec
7672	Gabbro	Gabbro	15.8	No	10 µm/sec
7673	Gabbro	Gabbro	15.8	No	10 µm/sec
7674	Gabbro	Gabbro	15.8	No	1 µm/sec
7675	Gabbro	Gabbro	15.8	No	1 µm/sec
7676	Gabbro	Gabbro	15.8	No	0.25 µm/sec
7680	Gabbro	Gabbro	19.0	No	10 µm/sec
7681	Gabbro	Gabbro	19.0	No	10 µm/sec
7682	Gabbro	Gabbro	19.0	No	10 µm/sec
7683	Gabbro	Gabbro	19.0	No	5 µm/sec
7684	Gabbro	Gabbro	19.0	No	5 µm/sec
7685	Gabbro	Gabbro	19.0	No	2 µm/sec
7686	Gabbro	Gabbro	19.0	No	2 µm/sec
7687	Gabbro	Gabbro	19.0	No	1 µm/sec
7688	Gabbro	Gabbro	19.0	No	1 µm/sec
7689	Gabbro	Gabbro	19.0	No	0.5 µm/sec
7690	Gabbro	Gabbro	18.9	No	0.5 µm/sec
7691	Gabbro	Gabbro	18.9	No	0.25 µm/sec
7692	Gabbro	Gabbro	18.9	No	0.25 µm/sec
7693	Gabbro	Gabbro	18.9	No	1 µm/sec
7694	Gabbro	Gabbro	18.9	No	2 µm/sec
7695	Gabbro	Gabbro	18.9	No	5 µm/sec
7696	Gabbro	Gabbro	18.9	No	10 µm/sec
7697	Gabbro	Gabbro	18.9	No	15 µm/sec
7698	Gabbro	Gabbro	18.9	No	12 µm/sec
7700	Gabbro	Dolomite	15.7	No	1 µm/sec

7701	Gabbro	Dolomite	15.7	No	10 μm/sec
7702	Gabbro	Dolomite	15.7	No	10 μm/sec
7703	Gabbro	Dolomite	15.7	No	1 μm/sec
7704	Gabbro	Dolomite	15.7	No	1 μm/sec
7705	Gabbro	Dolomite	15.7	No	0.5 μm/sec
7706	Gabbro	Dolomite	15.7	No	0.25 μm/sec
7707	Gabbro	Dolomite	15.7	No	0.25 μm/sec
7708	Gabbro	Dolomite	15.7	No	0.5 μm/sec
7709	Gabbro	Dolomite	15.7	No	1 μm/sec
7710	Gabbro	Dolomite	15.7	No	2 μm/sec
7711	Gabbro	Dolomite	15.7	No	5 μm/sec
7712	Gabbro	Dolomite	15.7	No	5 μm/sec
7713	Gabbro	Dolomite	15.7	No	5 μm/sec
7714	Gabbro	Dolomite	15.4	No	10 μm/sec
7715	Gabbro	Dolomite	15.7	No	10 μm/sec
7716	Gabbro	Dolomite	15.5	Yes	1 μm/sec
7717	Gabbro	Dolomite	15.6	Yes	1 μm/sec
7718	Gabbro	Dolomite	15.5	Yes	0.25 μm/sec
7719	Gabbro	Dolomite	15.5	Yes	0.25 μm/sec
7720	Gabbro	Dolomite	15.5	Yes	10 μm/sec
7721	Gabbro	Dolomite	15.6	Yes	10 μm/sec
7722	Gabbro	Dolomite	15.6	Yes	10 μm/sec
7723	Gabbro	Dolomite	15.6	Yes	10 μm/sec
7730	Dolomite	Gabbro	14.8	No	10 μm/sec
7731	Dolomite	Gabbro	14.6	No	10 μm/sec
7732	Dolomite	Gabbro	14.6	No	1 μm/sec
7733	Dolomite	Gabbro	14.7	No	1 μm/sec
7734	Dolomite	Gabbro	14.8	No	0.25 μm/sec
7735	Dolomite	Gabbro	14.8	No	10 μm/sec
7736	Dolomite	Gabbro	14.8	No	100 μm/sec
7737	Dolomite	Gabbro	14.8	No	100 μm/sec
7738	Dolomite	Gabbro	14.8	No	0.25 μm/sec
7740	Gabbro	Dolomite	15.7	No	10 μm/sec
7741	Gabbro	Dolomite	15.7	No	10 μm/sec
7742	Gabbro	Dolomite	15.7	No	10 μm/sec
7743	Gabbro	Dolomite	15.7	No	100 μm/sec
7744	Gabbro	Dolomite	15.7	Yes	100 μm/sec
7745	Gabbro	Dolomite	15.7	Yes	100 μm/sec
7746	Gabbro	Dolomite	15.7	No	10 μm/sec
7747	Gabbro	Dolomite	15.6	No	1 μm/sec
7748	Gabbro	Dolomite	15.6	Yes	0.25 μm/sec
7749	Gabbro	Dolomite	15.6	Yes	100 μm/sec

Note: Experiment numbers 7600 and later have two accelerometers on both sides; accelerometers 91 and 96 are on the top block, while accelerometers 90 and 93 are on the bottom block.

Appendix E Spectral Ratio Analysis

I calculated spectral ratios for a more quantitative comparison between two events. Spectral ratios are a good tool for seeing which frequencies two events are similar and where they are different. I have calculated two spectral ratios (Figures E.1 and E.2). The plots are a log-log plot of frequency vs ratio amplitude; the plot is colored black when the two events have similar frequency content and the plot is red or blue where the events have different frequency content. Further, if the plot is red the event in the numerator has a greater amplitude at that frequency and if the plot is blue the event in the denominator has a greater amplitude at that frequency.

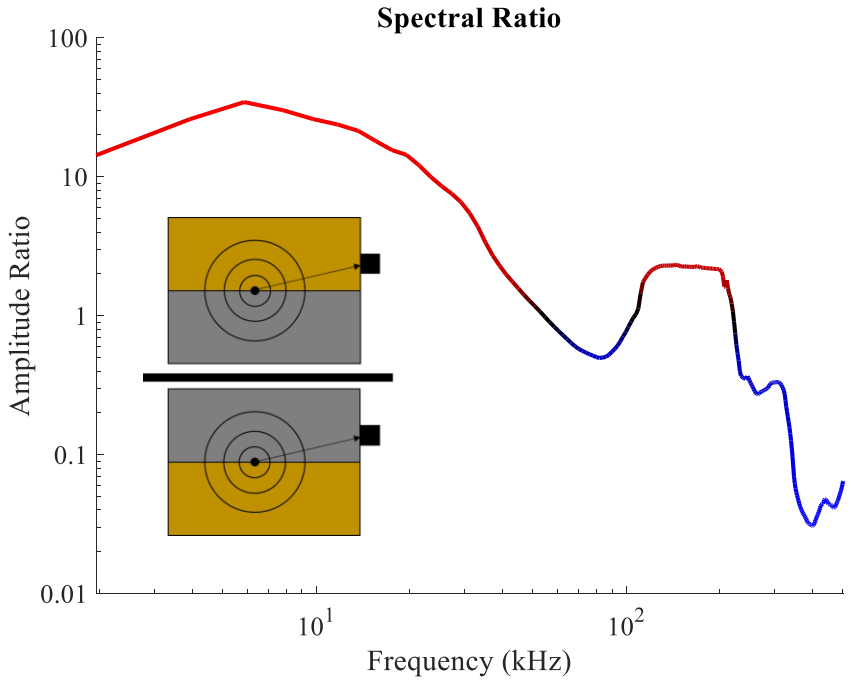

Figure E.1 Spectral ratio of two events from SS-GB (Figure 4.3) and GB-SS (Figure 4.4) experiments.

I have calculated the spectra ratio (Figure E.1) of the two events from SS-GB (Figure 4.3) and GB-SS (Figure 4.4) experiments. The results show that when the recording block is SS there is higher amplitude at lower frequencies and when the recording block is GB there is higher

amplitude at higher frequencies. Again, the difference in frequency content must be due to the path effect.

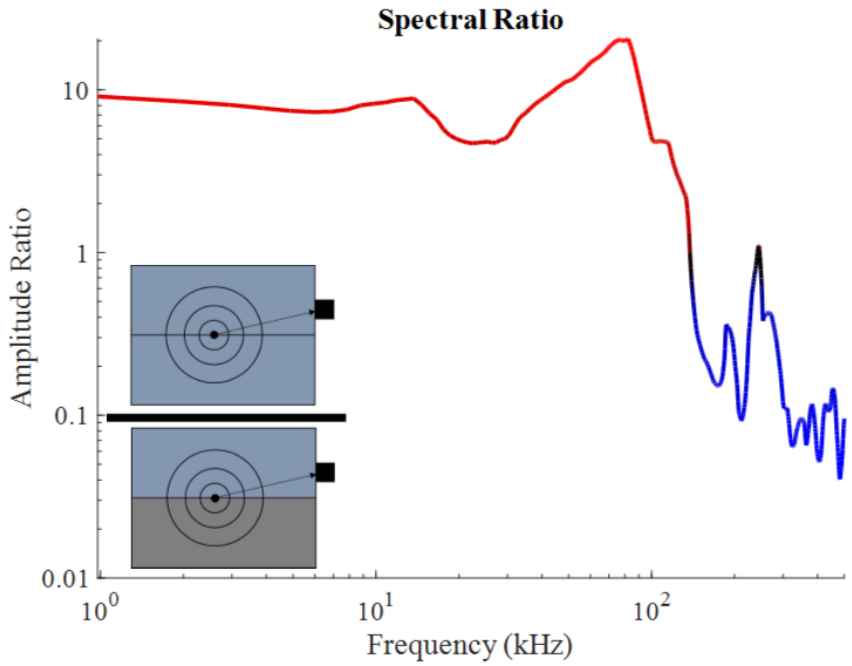

Figure E.2 Spectral ratio of two event from DOL-DOL (Figure 4.5) and DOL-GB (Figure 4.6) experiments.

I also calculated the spectral ratio (Figure E.2) of the two events from DOL-DOL (Figure 4.5) and DOL-GB (Figure 4.6) experiments. The results show that the amplitude is higher at lower frequencies for the event created by the DOL-DOL contact and that the amplitude is higher at higher frequencies for the event created by the DOL-GB contact. Again, the difference in frequency content is due to the source characteristics.

Appendix F Direct Comparison of Wave Propagation Path

The addition of the slow motor to ROGA has allowed for accelerometers to be epoxied on both blocks during shear because of low displacement. This allows for the direct comparison of an event on either side of the fault. For example, I sheared DOL-GB and recorded an acoustic event on the DOL (Figure F.1A) and that same event on the GB (Figure F.1B). The accelerometers are approximately equal distances from the fault. The differences in waveforms between the two recording are due to ray path. Preliminary results show a distinct difference in both peak amplitude and frequency content between the two events. The higher peak amplitude (250g) was recorded on the DOL, while peak amplitude recorded on gabbro was only 75g.

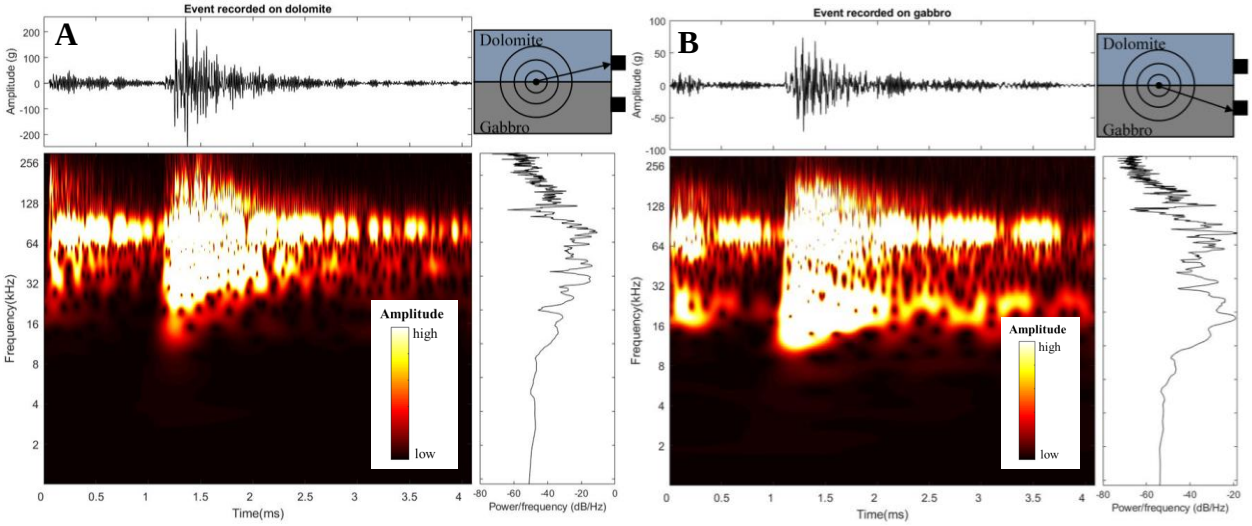

Figure F.1 Accelerogram, spectrogram, and power spectrum of an acoustic emission recording on both sides of the experimental fault in a dolomite-gabbro experiment. (A) Event recorded on the dolomite, where the peak amplitude is 250g. (B) Event recorded on the gabbro, where the peak amplitude is 75g. The frequency band at ~80 kHz in both recordings is due to machine response and is ignored for comparisons.

The difference in peak amplitude of the two recordings on either side of the fault suggests that the event was not created on the fault surface. Furthermore, since the peak amplitude is greater in the dolomite recording, the failure mechanism is likely cracking in the dolomite and not asperity failure at the fault contact. The decrease in peak amplitude seen in the gabbro

recording is likely due to the energy not being transmitted at the fault contact because of the impedance contrast.